A New Entropy Estimation Method for Dual-Polarimetric SAR Data: Comparative Analysis With Quad- and Other Dual-Polarization Approaches

Liting Liang, *Member, IEEE*, Yunhua Zhang, *Member, IEEE*, Dong Li, *Member, IEEE*, and Xiao Dong, *Member, IEEE*

***Abstract*—This article proposes a new method for estimating target polarimetric entropy from dual-polarimetric (DP) synthetic aperture radar (SAR) data based on the reciprocity assumption commonly applied in the processing of full-polarimetric (FP) SAR data. By applying matrix analysis theory, an explicit mathematical relationship is established between the proposed DP entropy and the widely used FP entropy, based on which relationships among existing DP entropies and the FP entropy are also elucidated theoretically. Comparative experiments using FP data from San Francisco acquired by Gaofen-3 and Radarsat-2, along with DP data from the same region acquired by Sentinel-1, validate the efficacy of the theory and demonstrate the superiority of the proposed entropy in characterizing the randomness of target polarimetric scattering, which, compared to existing DP entropies, showcases better consistency with the target FP scattering characteristics and better performance for target classification in terms of both overall accuracy and reliability. Highly consistent results are also observed in the experiment based on AIRSAR data from Flevoland, which primarily focuses on analyzing the performances of DP entropies across various types of crops with low-to-medium FP entropy. Besides, this better target discrimination property of the proposed entropy also leads to its more accurate result in landslide detection, improving the capability for target feature description and disaster monitoring using DP data effectively. It is worth noting that while we apply the proposed theory to the DP data of Sentinel-1, the theoretical analysis approach is universally applicable to other DP modes as long as reciprocity holds.**

***Index Terms*—Dual-polarimetric (DP) synthetic aperture radar (SAR), matrix analysis, polarimetric scattering entropy, reciprocity theorem, Sentinel-1 data.**

Manuscript received 10 March 2024; revised 21 May 2024; accepted 18 June 2024. Date of publication 21 June 2024; date of current version 8 July 2024. This work was supported in part by the China Postdoctoral Science Foundation under Grant 2022M723173, in part by the National Natural Science Foundation of China under Grant 42301466, and in part by the 2022 Youth Innovation Project of National Space Science Center, Chinese Academy of Sciences under Grant E2PD4001. *(Corresponding author: Liting Liang.)*

Liting Liang is with the CAS Key Laboratory of Microwave Remote Sensing, National Space Science Center, Chinese Academy of Sciences, Beijing 100190, China (e-mail: liangliting@mirslab.cn).

Yunhua Zhang, Dong Li, and Xiao Dong are with the CAS Key Laboratory of Microwave Remote Sensing, National Space Science Center, Chinese Academy of Sciences, Beijing 100190, China, and also with the School of Electronic, Electrical and Communication Engineering, University of Chinese Academy of Sciences, Beijing 100049, China (e-mail: zhangyunhua@mirslab.cn; lidong@mirslab.cn; dongxiao@mirslab.cn).

Digital Object Identifier 10.1109/JSTARS.2024.3417469

I. Introduction

Compared to full-polarimetric (FP) synthetic aperture radar (SAR) systems that can capture the complete polarimetric scattering information of the remotely sensed target [1], [2], dual-polarimetric (DP) SAR systems have gained a wider range of Earth observation applications due to distinct advantages in cost, system complexity, observation scale, etc. [3], [4], [5]. However, with only partial polarimetric information, it is challenging to extract polarimetric features with clear physical significance from the DP data for target interpretation [6], [7]. Numerous studies have been dedicated to identifying polarimetric features from DP information that are consistent with their FP counterparts [8], [9], [10]. This is not only because parameters extracted from FP data more realistically reflect the target features and the related research is more comprehensive, but also aims to deeply explore the potential of DP information, thereby enabling more effective and diverse applications, e.g., biomass mapping, forest evolution monitoring, soil moisture retrieval, and permanent water body identification [5]. Among them, the most indispensable and frequently applied parameter is the polarimetric entropy, initially proposed based on the FP data [11] and later introduced into the DP case by Cloude [7]. Due to its capability to accurately reflect the depolarization statistics of targets, the FP entropy has found extensive use in applications such as terrain/land-use classification and target recognition [12], [13], [14]. Besides, it has demonstrated a significant advantage in change detection compared to other polarimetric parameters [15], [16]. Since the target depolarization feature can also be reflected in its DP data [7], and given the growing importance of environmental surveillance based on DP SAR missions, such as Sentinel-1 [17], [18], [19], the estimation of entropy from DP data holds great promise for various applications [20], [21], [22], [23]. It is worth noting that the other two regularly used DP features of the target [10], [24], [25], anisotropy and degree of polarization, essentially possess the same information as the DP entropy [10], further corroborating the significant role the DP entropy plays in target feature analysis.

However, there is a crucial debate on the definition of entropy for DP data, i.e., there are two different estimation methods

proposed by Cloude [7], and Ji and Wu [8], respectively. The former has been mostly adopted, such as in maritime target detection [20], vegetation classification [26], and agricultural monitoring [22], while the latter has also been applied to soil state identification [19], persistent scatterer analysis [27], and so on [17]. Nevertheless, there is a lack of theoretical analysis and comparison between these two methods. The characteristics of each method in target recognition are not yet clear, making it difficult to fully leverage their respective advantages. More importantly, it is known that partial information in FP data is shared with DP data, and FP and DP entropies share the same physical significance, but the relationship between different entropies has not been studied theoretically and quantitatively so far, even though many studies have compared their performances experimentally [15], [16]. These issues seriously affect our knowledge of the DP entropy and impede its effective applications based on theoretical guidance. In addition, the performances of existing DP entropies in discerning targets and detecting changes are also unsatisfactory, as indicated by related research [3], [15], [20], even though they have been adopted by most DP data applications. Therefore, both in terms of theoretical analysis and practical applications, significant gaps and challenges still exist in the research on DP entropy.

To address the aforementioned issues, this article conducts research on the estimation method of target polarimetric entropy based on DP data. We propose a new scattering vector model for target DP information based on the reciprocity assumption commonly applied in FP data processing, and then a new entropy is derived according to its definition. According to the connection between the new DP and the FP scattering vectors, explicit mathematical relationships can be established between the proposed DP entropy and the widely used FP entropy by applying matrix analysis theory, and based on which, relationships among existing DP and FP entropies can also be clarified theoretically. The theory efficacy is verified by comparative experiments using San Francisco FP data acquired by Gaofen-3 and Radarsat-2 and DP data acquired by Sentinel-1. The performances of different entropies on various targets are analyzed both theoretically and experimentally, demonstrating the superiority of the proposed entropy in characterizing the randomness of target polarimetric scattering compared to existing DP entropies. Meanwhile, factors contributing to the difference between the FP and the DP entropies are discussed systematically to provide insight into their divergence and offer guidance for DP entropy application in future contexts. Similar results are observed in the experiment based on Airborne SAR (AIRSAR) data from Flevoland, which primarily focuses on analyzing the performances of DP entropies across various crops with low-to-medium FP entropy. Besides, the experiment using Sentinel-1 data acquired before and after the 2022 Luding earthquake [28] further implies that a more accurate result in landslide detection can be obtained with the proposed DP entropy due to its better target discrimination capability.

It needs to be clarified that since the proposed method is based on the reciprocity assumption, its applicability is subject to the validity conditions of the reciprocity theorem. Nonetheless, considering that reciprocity is a basic assumption always made in FP SAR data processing [29] as nonreciprocal backscatter problems are not common in the remote sensing of natural land and sea surfaces [2], and experiments in the article prove the validity of the reciprocity theorem, the proposed method has wide applicability.

The rest of this article is organized as follows. Section II introduces the definition of the target FP entropy, along with existing and proposed methods for target DP entropy estimation. The theoretical analysis of their relationships is presented in Section III and Section IV validates it by processing multiple sets of FP and DP data and analyzes the performances of different entropies on various targets. Section V further compares DP entropies on various low-to-medium FP entropy crops using AIRSAR data, and in Section VI, they are applied to landslide detection. Some key points related to the work are discussed in Section VII. Finally, Section VIII concludes this article.

II. Polarimetric Entropy Estimation

A. Entropy Estimation From FP Data

The fully polarimetric scattering of a pure/single target can be modeled by the scattering matrix

$$[S] = \begin{bmatrix} S_{HH} & S_{VH} \\ S_{HV} & S_{VV} \end{bmatrix} \tag{1}$$

where the first and second letters of the matrix element subscript represent the transmitted and received polarizations, respectively. Under the reciprocity condition $S_{HV} = S_{VH}$ [1], [2], [30], the Lexicographic feature vector is obtained as

$$\boldsymbol{c} = \begin{bmatrix} S_{HH} & \sqrt{2}S_X & S_{VV} \end{bmatrix}^{\mathrm{T}} \tag{2}$$

where the superscript T denotes transposition operation. Although S_X shown in (2) is always written as S_{HV}, in practical FP SAR data processing it is obtained by

$$S_X = \frac{S_{HV} + S_{VH}}{2} \tag{3}$$

serving as the cross-polarization component of the target scattering [1], [2], [31]. The target covariance matrix is then expressed as

$$\begin{aligned} [C] &= \langle \boldsymbol{c} \cdot \boldsymbol{c}^{*\mathrm{T}} \rangle \\ &= \left\langle \begin{bmatrix} |S_{HH}|^2 & \sqrt{2}S_{HH}S_X^* & S_{HH}S_{VV}^* \\ \sqrt{2}S_X S_{HH}^* & 2|S_X|^2 & \sqrt{2}S_X S_{VV}^* \\ S_{VV}S_{HH}^* & \sqrt{2}S_{VV}S_X^* & |S_{VV}|^2 \end{bmatrix} \right\rangle \\ &= \begin{bmatrix} C_{11} & C_{12} & C_{13} \\ C_{12}^* & C_{22} & C_{23} \\ C_{13}^* & C_{23}^* & C_{33} \end{bmatrix} \end{aligned} \tag{4}$$

where $\langle \cdot \rangle$ denotes ensemble average.

The polarimetric entropy H is defined as the degree of statistical disorder of each distinct scatter type within the ensemble [1],

[2], which is given by

$$H = -\sum_{i=1}^{3} p_i \log_3 p_i \tag{5}$$

where p_i corresponds to the pseudoprobability obtained from the eigenvalue λ_i of $[C]$

$$p_i = \frac{\lambda_i}{\sum_{j=1}^{3} \lambda_j} = \frac{\lambda_i}{\text{SPAN}} \quad (i = 1, 2, 3) \tag{6}$$

and SPAN is the target total power. Since $[C]$ is a Hermitian positive semidefinite matrix, we adopt the convention that its eigenvalues are arranged in algebraically nonincreasing order that $\lambda_1 \geq \lambda_2 \geq \lambda_3 \geq 0$.

B. DP Scattering Vector Model and Entropy Estimation

Similarly, the entropy of the DP data is extracted from the eigenvalues of the DP covariance matrix, which is constructed by the target DP scattering vector [7], [8].

Let us take the second column of $[S]$ as the data obtained by the DP SAR system (it is the case for Sentinel-1). Cloude constructs the scattering vector directly under Lexicographic basis as $\boldsymbol{c}_C = [S_{VV} \quad S_{VH}]^{\mathrm{T}}$ [7], and the covariance matrix is $[C_C] = \langle \boldsymbol{c}_C \cdot \boldsymbol{c}_C^{*\mathrm{T}} \rangle$. On the other hand, Ji and Wu adopt $\boldsymbol{c}_J = [S_{VV} \quad 2S_{VH}]^{\mathrm{T}}$ as the DP scattering vector [8] to construct the covariance matrix $[C_J]$.

Different from the two, this article proposes a new scattering vector model in order to represent the DP observation more approximate to the target FP scattering characteristic, as

$$\boldsymbol{c}_L = \left[S_{VV} \quad \sqrt{2} S_{VH} \right]^{\mathrm{T}} \tag{7}$$

and the covariance matrix is

$$[C_L] = \langle \boldsymbol{c}_L \cdot \boldsymbol{c}_L^{*\mathrm{T}} \rangle = \left\langle \begin{bmatrix} |S_{VV}|^2 & \sqrt{2} S_{VV} S_{VH}^* \\ \sqrt{2} S_{VH} S_{VV}^* & 2|S_{VH}|^2 \end{bmatrix} \right\rangle. \tag{8}$$

Note that the form of $\boldsymbol{c}_L$ comes from the widely accepted reciprocity assumption in FP information processing, which is often used as $S_{HV} = S_{VH}$ in the scattering matrix of a monostatic radar in the HV polarization basis [30]. Nonreciprocal backscatter problems, which may arise due to propagation effects (such as Faraday rotation), interaction with special materials, or potentially measurement noise [32], are uncommon in the remote sensing of natural land and sea surfaces [2]. Thus, the reciprocity assumption, which holds true in the vast majority of cases, is fundamental and crucial for the processing of FP SAR data [1], [30]. It is important to recognize that Faraday rotation represents an important exception that affects the validity of the reciprocity theorem, yet this phenomenon primarily impacts low-frequency (L- or P-band) spaceborne SAR systems to a certain extent [1], [2]. In summary, the applicability of $\boldsymbol{c}_L$ is aligned with the conditions under which the reciprocity assumption can be made, and subsequent experiments will be conducted using C-band spaceborne and L-band airborne SAR data, which are less affected by Faraday rotation [1], [2], [29].

Accordingly, when the reciprocity theorem $S_{HV} = S_{VH}$ holds, it is reasonable to think the DP data contains the information of S_{HV} with a virtual total power of

$$\begin{aligned} \text{SPAN}_L &= \langle |S_{VV}|^2 \rangle + \langle |S_{VH}|^2 \rangle + \langle |S_{HV}|^2 \rangle \\ &= \langle |S_{VV}|^2 \rangle + 2\langle |S_{VH}|^2 \rangle. \end{aligned} \tag{9}$$

The factor $\sqrt{2}$ in (7) ensures the power consistency of (8) and (9), which has a clear physical significance and does not deviate from the actual polarimetric scattering characteristics of the target.

Different DP entropies will be obtained based on different scattering vectors [7], [8], and as for the proposed $\boldsymbol{c}_L$ case, H_L can be expressed as (see Appendix A for the detailed derivation)

$$H_L = -p_L \log_2 p_L - (1 - p_L) \log_2 (1 - p_L) \tag{10}$$

where p_L is the maximum pseudoprobability obtained from λ_L, the maximum eigenvalue of $[C_L]$, i.e.,

$$p_L = \frac{\lambda_L}{\text{SPAN}_L} \quad \left(\frac{1}{2} \leq p_L \leq 1 \right). \tag{11}$$

According to (10), H_L is uniquely determined by p_L and is monotonically decreasing over p_L. The same can be derived for the DP entropies proposed by Cloude (H_C) and Ji and Wu (H_J). Therefore, the theoretical analysis of DP entropies hereinafter will be replaced by that of their maximum pseudoprobabilities, which have explicit analytical expressions.

III. Theoretical Analysis of FP and DP Entropies

In this section, relationships between the FP entropy H and DP entropies H_C, H_J, and H_L are discussed and illustrated by data simulation, and a detailed description of the simulation steps is given in Appendix B. Note that the following theoretical analysis is performed under the reciprocity assumption, which represents the ideal observation of reciprocal targets by a monostatic backscatter polarimetric SAR system.

A. Relationships Between DP Entropies H_C, H_J, and H_L

According to (7)–(11), the analytical expression of p_L can be derived, and those of p_C and p_J can be obtained similarly, which can be written as (see Appendix A for the detailed derivation)

$$p_C = \frac{1}{2} + \frac{\sqrt{(r_C - \frac{1}{2})^2 + 2r_X}}{2(r_C + \frac{1}{2})} \tag{12}$$

$$p_J = \frac{1}{2} + \frac{\sqrt{(r_C - 2)^2 + 8r_X}}{2(r_C + 2)} \tag{13}$$

$$p_L = \frac{1}{2} + \frac{\sqrt{(r_C - 1)^2 + 4r_X}}{2(r_C + 1)} \tag{14}$$

where

$$\begin{cases} r_C = \frac{\langle |S_{VV}|^2 \rangle}{2\langle |S_{VH}|^2 \rangle} \\ r_X = \frac{|\langle S_{VV} S_{VH}^* \rangle|^2}{2\langle |S_{VH}|^2 \rangle^2} \end{cases}, \quad r_C \geq r_X \geq 0 \tag{15}$$

and in the case of reciprocity, we have $r_C = C_{33}/C_{22}$ and $r_X = |C_{23}|^2/C_{22}^2$, i.e., for any given FP covariance matrix of

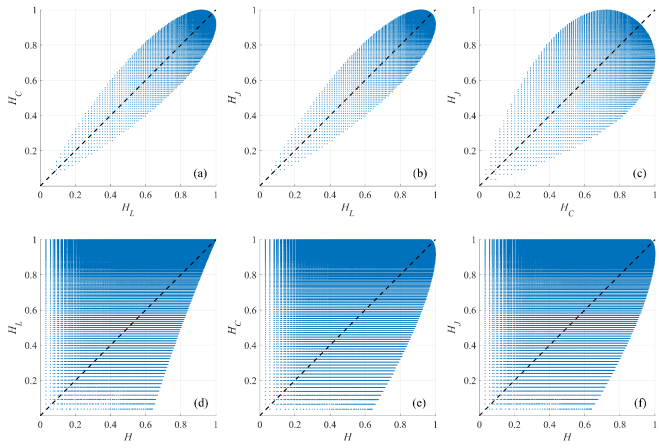

Fig. 1. Simulation results of the relationships between different entropies, where the first row shows the relationships among DP entropies, i.e., (a) H_C and H_L, (b) H_J and H_L, and (c) H_J and H_C, and the second row compares DP entropies with FP entropy, respectively, i.e., (d) H_L and H, (e) H_C and H, and (f) H_J and H. The black dashed line of each figure is the angle bisector of the two axes.

a target, p_C, p_J, and p_L can be directly calculated. On the other hand, when p_L is known, the ranges of p_C and p_J can be determined separately by considering possible values of r_C and r_X. Accordingly, relationships between H_C, H_J, and H_L can be established, as shown in Fig. 1(a), (b), and (c). In general, they are highly linearly correlated. It can be observed that they share the same definition for the single target, i.e., they all equal 0 when $r_C = r_X$. However, as the difference between r_C and r_X emerges, variations also occur. For the random target, H_C, H_J, and H_L have different definitions due to differences in their covariance matrix forms, i.e., $H_C = 1$ when $r_C = 1/2$ and $r_X = 0$, $H_J = 1$ when $r_C = 2$ and $r_X = 0$, and $H_L = 1$ when $r_C = 1$ and $r_X = 0$.

Besides, the following relationship can also be derived

$$H_C \leq H_L, \quad \text{when } r_C \geq \sqrt{2}/2 \tag{16}$$

$$H_C \leq H_J, \quad \text{when } r_C \geq 1 \tag{17}$$

$$H_L \leq H_J, \quad \text{when } r_C \geq \sqrt{2} \tag{18}$$

which will be further discussed in the experiments.

B. Relationship Between H_L and H

Undoubtedly, it is impossible to find an exact expression between DP entropy and FP entropy because of the missing information of DP data compared with FP data. However, considering the common entries of DP and FP covariance matrices, it is possible to predict the performance of DP entropy at a given H to some extent. The relationship between H_L and H is discussed first based on theorems of matrix analysis.

As shown in (4) and (8), under the reciprocity assumption $S_{HV} = S_{VH}$, $[C_L]$ is a principal submatrix of $[C]$. Therefore, their eigenvalues have the following inequality relationship according to Cauchy's interlacing theorem [33]

$$\lambda_1 \geq \lambda_L \geq \lambda_2 \geq \text{SPAN}_L - \lambda_L \geq \lambda_3 \tag{19}$$

which can be expressed in the form of pseudoprobability as

$$p_1 \geq p_L \cdot r_S \geq p_2 \geq (1 - p_L) \cdot r_S \geq 1 - p_1 - p_2 \tag{20}$$

where

$$r_S = \frac{\text{SPAN}_L}{\text{SPAN}} \quad (0 \leq r_S \leq 1) \tag{21}$$

reflects the power relationship between the DP and the FP data. The relationship between the main diagonal entries and the eigenvalues of a Hermitian matrix given by Schur further restricts the range of r_S [33], as

$$1 - p_1 \leq r_S \leq p_1 + p_2. \tag{22}$$

With the above restrictions, the range of p_L can be derived as a function of p_1, p_2, and r_S

$$\max\left\{\frac{p_2}{r_S}, 1 - \frac{p_2}{r_S}\right\} \leq p_L \leq \min\left\{\frac{p_1}{r_S}, 1 - \frac{1 - p_1 - p_2}{r_S}\right\}. \tag{23}$$

Since H is determined by p_1 and p_2, (23) illustrates that the only uncertain factor between H and H_L is r_S, which is also influenced by p_1 and p_2.

Accordingly, the relationship between H_L and H can be deduced, as shown in Fig. 1(d). Overall, although there is uncertainty in the values of H_L for any given H, the correlation between H_L and H can be clearly identified, and the uncertainty between them decreases as H increases. Specifically, when H is less than 0.6309, H_L can take any value within the [0, 1] range. And their difference reduces to 0 when $H = 1$, which is a sufficient condition for $H_L = 1$. Note that the 0.6309 can be derived from another perspective, i.e., the maximum value H can achieve when $H_L = 0$. Since $H_L = 0$ means $p_L = 1$, and by substituting it into (20), the constraint $p_1 + p_2 = 1$ can be obtained. Accordingly, the maximum value of H in this case can be deduced to be 0.6309.

This phenomenon can also be explained in terms of physical significance. On the one hand, a small H value implies low polarimetric randomness in the target scattering, and maybe one scattering mechanism dominates the FP covariance matrix. In this case, the correlation between the corresponding scattering vector and the lost information of the DP data determines H_L, which can be any value within [0, 1]. On the other hand, a large H value indicates that the target with high scattering randomness has three orthogonal scattering mechanisms with approximate power. In such a situation, its DP covariance matrix also preserves the feature as a principal submatrix of the FP covariance matrix, and H_L will also be large.

C. Relationships Between H_C, H_J, and H

Although no eigenvalue inequality can be applied to establish direct connections between p_C and p_J with H, as demonstrated in the preceding section, (12)–(14) can be employed to convey the constraint (23) on p_L to them. Fig. 1(e) and (f) illustrate the relationships between H_C and H and between H_J and H, respectively, which exhibit similar characteristics to that of H_L in general. However, when $H \geq 0.6309$, the ranges of the two for a given H are larger than that of H_L, showing greater

uncertainty. Besides, different from H_L, $H = 1$ is a sufficient condition for $H_C \neq 1$ and $H_J \neq 1$. In other words, both H_C and H_J are unable to attain their maximum values when H reaches its maximum value. This makes their interpretation of the completely random target inconsistent with that of H.

D. Discussions of Other DP Modes

While the above analysis takes the polarization mode of Sentinel-1 (VV-VH) as an example, the methodology and findings are equally applicable to other DP modes, namely, the HH-VV and the HH-HV modes. For the HH-VV mode, as there is no cross-polarization scattering information acquired, the entropy estimation methods by Cloude, Ji and Wu, and this article are the same. In this case, the relationship between the DP and the FP entropy is the same as that shown in Fig. 1(d). For the HH-HV mode, relationships of H_L, H_C, and H_J with H shown in Fig. 1(d), (e), and (f) still hold. It should be noted that definitions of r_C, r_X, and r_S vary for different DP modes.

IV. Experiment With Spaceborne C-Band FP and DP SAR Data From San Francisco

A. Theory Verification With Simulated DP Data

This part uses simulated DP data of VV and VH polarizations from FP data to verify the theoretical analysis above, as is commonly done in related research [21], [34], [35].

Two sets of FP SAR data of San Francisco obtained respectively by C-band spaceborne radar systems Gaofen-3 and Radarsat-2 are employed to demonstrate the universality of the theory. Before data processing, we calculate the Pearson product-moment correlation coefficient between S_X and S_{VH}, the cross-polarization components respectively employed by FP and DP data analysis, which is 0.9937 of the Gaofen-3 data and 0.9885 of the Radarsat-2 data, indicating the validity of the reciprocity assumption. For both the two data, the original single-look complex scattering matrix data is multilooked by 2 $\times$ 2 (in the range and azimuth) to generate the FP covariance matrix, then a 3 $\times$ 3 boxcar filter is applied to reduce the speckle noise. Same processing is done to obtain the DP covariance matrices based on $\boldsymbol{c}_C$, $\boldsymbol{c}_J$, and $\boldsymbol{c}_L$, respectively.

Scatterplots of the derived entropies are shown in Fig. 2, with theoretical boundaries extracted from Fig. 1(d), (e), and (f) in red dotted lines. It shows that with only several discrete points beyond the range, the conclusion for the ideal reciprocal target is effective for most of the simulated DP data due to the high correlation between the target cross-polarization components. Fig. 3 shows the optical image of the experimental area, which includes various land cover types. Images of entropies are shown in Fig. 4(a)–(h), where the first and second rows present the results of the Gaofen-3 and Radarsat-2 data, respectively, and from left to right are H, H_C, H_J, and H_L, respectively. Overall, the results of the two data are highly consistent, and considering their different resolution, observation time, incidence, etc., subtle differences in the following quantitative analysis are also reasonable. Since the FP and DP entropies have similar physical

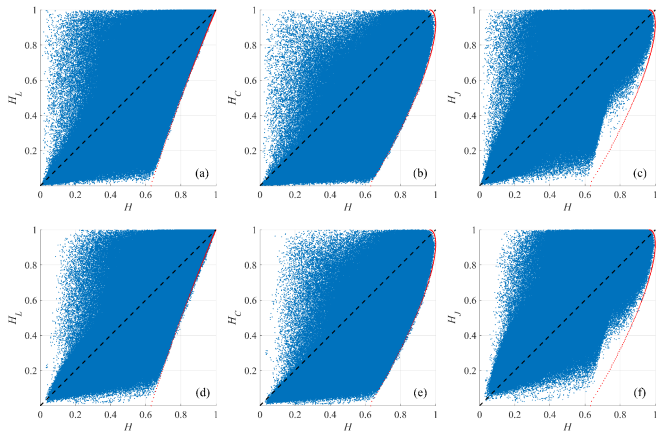

Fig. 2. Scatter diagrams comparing FP entropy H with DP entropies (a) and (d) H_L, (b) and (e) H_C, and (c) and (f) H_J, respectively. The first and second rows are the results of the Gaofen-3 and Radarsat-2 dada, respectively. The red dotted lines depict boundaries given by theoretical analysis, and the black dashed line of each figure is the angle bisector of the two axes.

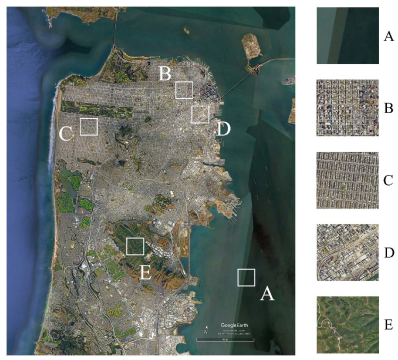

Fig. 3. Optical image of the experimental area in San Francisco, USA from Google Earth, with white squares marking five typical targets: the ocean (area A), the built-up areas with small, medium, and large polarization orientation angles (areas B, C, and D), and the vegetated region (area E).

significance [7], it is reasonable to observe their similar performances on specific targets, i.e., they are small for the ocean and lakes with single scattering mechanism, while they are almost 1 for parks and mountainous areas with strong volume scattering, and values of built-up areas are in between.

Fig. 4(a)–(h) show that H_L is much more consistent with H than H_C and H_J, and H_L appears larger than H_C while smaller than H_J. This can be further confirmed by Fig. 5, which shows the statistical histograms of the differences between H and DP entropies. Qualitatively, it can be explained from two aspects. On the one hand, it is known that $|S_{VH}|$ is usually much smaller than $|S_{VV}|$, so $[C_C]$ is closer to a rank-1 matrix than $[C_L]$ and $[C_J]$, with a higher p_C value and, therefore, a lower H_C value. On the other hand, the cross-polarization component S_{VH} is usually induced by complex building areas or natural targets classified as distributed target [1], [36], which will be apparently depolarized after the ensemble average. And $[C_J]$ constructed by $\boldsymbol{c}_J$ with $2S_{VH}$ enhances the depolarization effect compared with $[C_L]$ and $[C_C]$, so it leads to a larger entropy. Quantitatively, since most of the pixels (about 96% of the Gaofen-3 data and

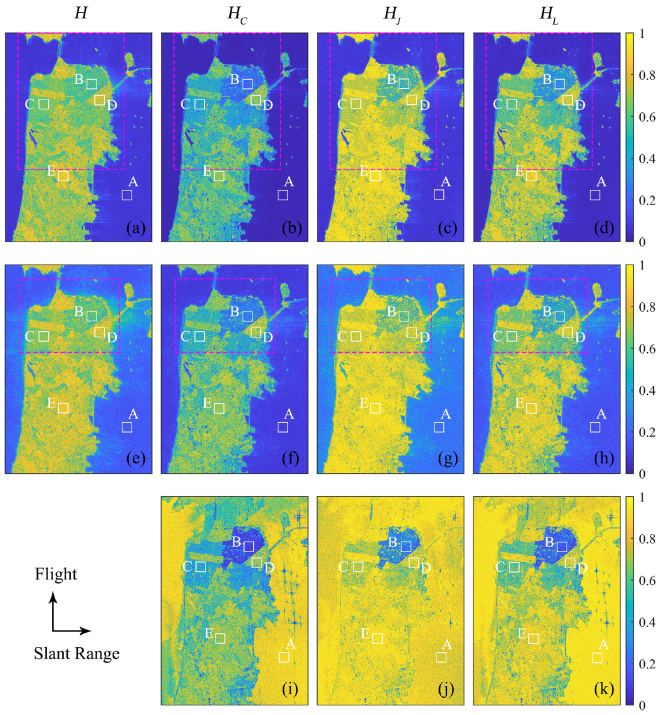

Fig. 4. Entropies derived from the (a)–(d) Gaofen-3, (e)–(h) Radarsat-2, and (i)–(k) Sentinel-1 data, respectively. From left to right, each column represents H, H_C, H_J, and H_L, respectively. The white squares mark the sample areas for the ocean region (A), the built-up areas with small, medium, and large POA (B, C, and D), and the vegetated region (E). The pink dashed rectangles in (a)–(h) indicate the classification zones of the Gaofen-3 and Radarsat-2 data.

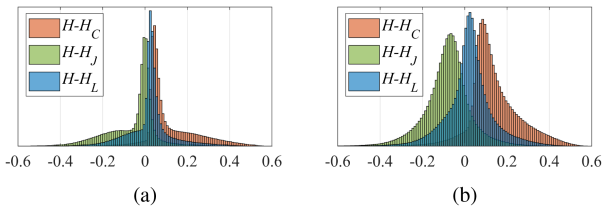

Fig. 5. Histograms of the differences between FP entropy H and DP entropies of the (a) Gaofen-3 and (b) Radarsat-2 data, respectively.

92% of the Radarsat-2 data statistically) satisfy the condition that $r_C \geq \sqrt{2}$, according to (16)–(18), the phenomenon $H_C \leq H_L \leq H_J$ is obvious.

Furthermore, taking H as the reference, we compute the mean absolute difference (MAD), root mean square of the difference (RMSD), and the coefficient of determination R^2 of H_C, H_J, and H_L, respectively. As listed in the third column of Table I, compared with H_C and H_J, H_L holds the smallest MAD and RMSD and the largest R^2 on both the Gaofen-3 and Radarsat-2 data, and this conforms with the results shown in Fig. 5, showing its best consistency with the FP entropy. Besides, statistical analysis is also conducted on sample areas to quantitatively evaluate their performances on various targets. Five kinds of typical targets in the scene are marked as shown in Fig. 3, i.e., the ocean (area A), built-up areas with small, medium, and large polarization orientation angle (POA) (areas B, C, and D) [37],

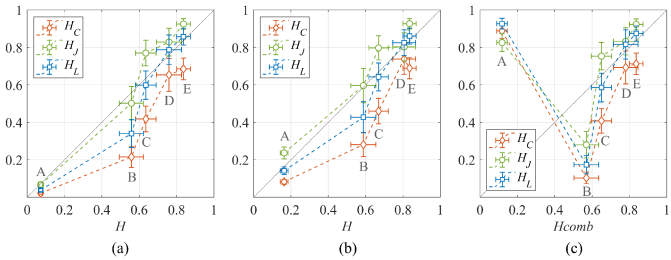

Fig. 6. Relationships between H and DP entropies on sample areas of the (a) Gaofen-3, (b) Radarsat-2, and (c) Sentinel-1 data, respectively.

[38], and vegetated region (area E). Columns 4 to 8 of Table I show the MAD and RMSD for sample areas A-E. R^2 is not used here because it provides more information when evaluating regression analysis rather than analysis of sample data with the same characteristics, and the nonlinear relationship between FP and DP entropies could lead to the meaningless result $R^2 < 0$ [39]. Nevertheless, using the MAD and RMSD is sufficient to reflect the cognitive differences between FP and DP entropies on different targets. Specifically, compared to H_C and H_J, the proposed DP entropy H_L exhibits higher consistency with H in sample areas C, D, and E for both datasets. For the ocean area A, H_J and H_L each perform optimally on Gaofen-3 and Radarsat-2 data, respectively. However, since the MAD and RMSD for all three DP entropies are very small, their differences in ocean areas are not significant. It is interesting to note that H_J shows higher consistency with H only for the small POA built-up area B. This is easy to explain by visualizing the relationships between H and DP entropies on the sample areas, as shown in Fig. 6(a) and (b), which respectively compare DP entropies with H in the sample areas from Gaofen-3 and Radarsat-2 data with error bars provided. It indicates that H_C and H_L in area B are significantly lower than H, hence the higher entropy estimation of H_J is closer to H. A detailed analysis of this phenomenon is provided in Sections IV-C and IV-D. Considering that the R^2 of H_L for the whole scene are larger than 0.8 of the two datasets, it is reasonable to take H_L as an effective descriptor of target polarimetric scattering randomness.

B. *Classification Experiment Based on Different Entropies*

Furthermore, a classification experiment is conducted to quantitatively compare the differentiation capability of different entropies on various targets. Fig. 7(a) and (b) present part of the ground truth maps of Gaofen-3 and Radarsat-2 data, respectively, with five kinds of targets marked: water body, urban areas with small, medium, and large POA, and vegetated regions [40]. However, as shown in Figs. 4 and 6, the four entropies, i.e., H, H_C, H_J, and H_L, fail to significantly differentiate between large POA urban area and vegetated region. Analysis of them using the Calinski–Harabasz criterion [41] led to the same conclusion: to avoid overfitting thus diminish target recognition capability of polarimetric entropy, the ideal clustering number is four. Accordingly, the classic k-means++ algorithm [42] is applied to cluster targets according to their entropy values into four

TABLE I
STATISTICAL DIFFERENCES BETWEEN FP ENTROPY AND DP ENTROPIES ON GAOFEN-3 AND RADARSAT-2 DATA

Data	DP Entropy	MAD / RMSD / R^2 (Overall)	MAD / RMSD				
			Area A	Area B	Area C	Area D	Area E
Gaofen-3	H_C	0.1237 / 0.1680 / 0.7166	0.0515 / 0.0541	0.3578 / 0.3818	0.2477 / 0.2792	0.1501 / 0.1806	0.1554 / 0.1747
	H_J	0.0824 / 0.1295 / 0.8315	**0.0161 / 0.0227**	**0.1740 / 0.2160**	0.1661 / 0.2072	0.1114 / 0.1385	0.0984 / 0.1166
	H_L	**0.0745 / 0.1111 / 0.8759**	0.0353 / 0.0385	0.2593 / 0.2902	**0.1462 / 0.1833**	**0.0893 / 0.1138**	**0.0542 / 0.0690**
Radarsat-2	H_C	0.1518 / 0.1835 / 0.5618	0.0822 / 0.0872	0.3167 / 0.3432	0.2350 / 0.2667	0.1239 / 0.1540	0.1499 / 0.1690
	H_J	0.1059 / 0.1355 / 0.7612	0.0736 / 0.0850	**0.1410 / 0.1777**	0.1576 / 0.1947	0.1034 / 0.1321	0.1004 / 0.1189
	H_L	**0.0821 / 0.1155 / 0.8264**	**0.0304 / 0.0383**	0.2044 / 0.2359	**0.1388 / 0.1720**	**0.0725 / 0.0985**	**0.0549 / 0.0697**

The boldface values serve to emphasize key results. Specifically, the boldface numbers indicate the optimal results among the different methods presented.

TABLE II
CLASSIFICATION RESULTS EVALUATION (%) WITH DIFFERENT ENTROPIES BASED ON GAOFEN-3 AND RADARSAT-2 DATA

Data	Entropy	Water Body	Small POA Urban	Medium POA Urban	Large POA Urban and Vegetated Region	Overall Accuracy	Kappa Coefficient
Gaofen-3	H	99.36	38.38	59.35	67.73	80.84	68.99
	H_C	**99.78**	64.10	43.78	53.79	78.89	65.47
	H_J	99.51	52.55	44.54	**80.22**	81.90	70.65
	H_L	99.70	**64.59**	**51.69**	71.02	**83.04**	**72.42**
Radarsat-2	H	77.70	21.26	61.44	81.04	66.31	52.57
	H_C	**97.53**	**55.27**	45.65	56.84	73.79	60.86
	H_J	76.78	30.20	39.55	**80.58**	62.98	47.94
	H_L	93.53	51.26	**52.80**	76.52	**76.09**	**64.92**

The boldface values serve to emphasize key results. Specifically, the boldface numbers indicate the optimal results among the different methods presented.

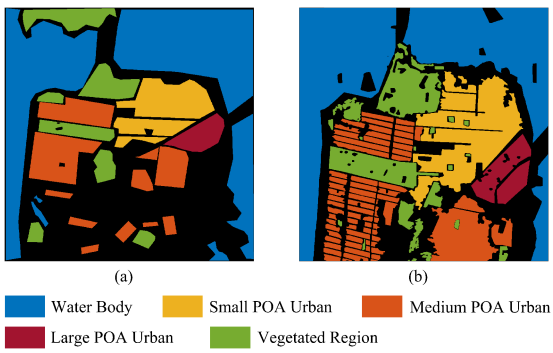

Fig. 7. Ground truth maps of the classified areas of the (a) Gaofen-3 and (b) Radarsat-2 data, respectively.

categories, respectively. And ordered by increasing centroid values, these categories correspond to water body, urban areas with small, medium, and large orientations/vegetated regions, respectively. The classification results of the four entropies are illustrated in Fig. 8 and detailed in Table II.

It can be observed that the proposed DP entropy H_L achieves the highest overall classification accuracy and kappa coefficient in both datasets. Moreover, compared to the other two DP entropies, H_L exhibits optimal or suboptimal performance across all four types of targets. In contrast, H_C and H_J show absolute advantages in identifying low entropy targets (water body) and high entropy targets (large POA urban areas/vegetated regions), respectively. This can be attributed to the general lower values of the former and higher values of the latter, resulting in weaker differentiation capabilities for various types of targets compared to H_L, as reflected by the kappa coefficients also. It is noteworthy that the classification performance of the FP entropy H does not always surpass that of DP entropies. This is primarily due to its lower recognition accuracy in small POA urban areas, and as aforementioned, this difference in performance between H and DP entropies will be analyzed in detail based on scattering mechanism in subsequent subsections. Nevertheless, the overall classification accuracy and kappa coefficient of H fall between those of H_C and H_J, and its performance in other classes of targets is at least superior to one DP entropy.

C. Experiment With Sentinel-1 DP Data

As aforementioned, the reciprocity assumption and the simulation of DP data using FP data represent an ideal situation of the polarimetric data, which can hardly be true in practice. Therefore, the data of the same area obtained by DP SAR Sentinel-1 is utilized in this part to further compare different DP entropies in real situations as well as examine the validity of the simulated DP data in Sections IV-A and IV-B.

Fig. 4(i)–(k) display the estimated H_C, H_J, and H_L from the Sentinel-1 data, respectively. Despite their high values of the ocean, which will be discussed later, the entropies of the

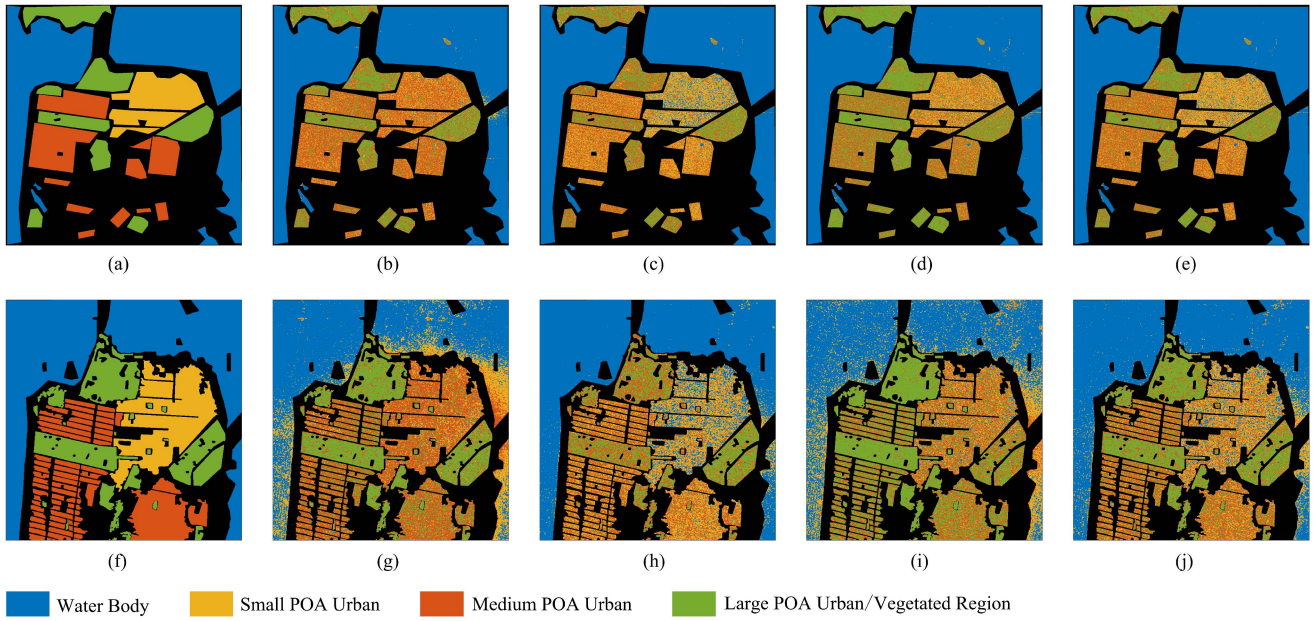

Fig. 8. Classification results of different entropies on Gaofen-3 (the first row) and Radarsat-2 (the second row) data, respectively. (a) and (f) Ground truth maps of four classes. Classification results of (b) and (g) H, (c) and (h) H_C, (d) and (i) H_J, and (e) and (j) H_L, respectively.

TABLE III
STATISTICAL CHARACTERISTICS OF DIFFERENT ENTROPIES IN SAMPLE AREAS OF GAOFEN-3, RADARSAT-2, AND SENTINEL-1 DATA

Data	Entropy	Mean / Standard Deviation				
		Area A	Area B	Area C	Area D	Area E
Gaofen-3	H	0.0725 / 0.0203	0.5584 / 0.1288	0.6355 / 0.1090	0.7595 / 0.1342	0.8372 / 0.0736
	H_C	0.0210 / 0.0093	0.2154 / 0.1117	0.4180 / 0.1368	0.6535 / 0.1761	0.6854 / 0.1162
	H_J	**0.0671** / 0.0272	**0.5019** / 0.1793	0.7702 / 0.1368	0.8289 / 0.1481	0.9254 / 0.0574
	H_L	0.0378 / 0.0162	0.3401 / 0.1501	**0.5988** / 0.1520	**0.7877** / 0.1572	**0.8575** / 0.0896
Radarsat-2	H	0.1639 / 0.0416	0.5880 / 0.1336	0.6693 / 0.1033	0.8063 / 0.1219	0.8352 / 0.0707
	H_C	0.0817 / 0.0250	0.2811 / 0.1284	0.4598 / 0.1367	0.7380 / 0.1634	0.6890 / 0.1124
	H_J	0.2364 / 0.0638	**0.5962** / 0.1842	0.7978 / 0.1290	**0.8029** / 0.1509	0.9273 / 0.0550
	H_L	**0.1411** / 0.0411	0.4275 / 0.1661	**0.6427** / 0.1487	0.8259 / 0.1372	**0.8609** / 0.0857
Sentinel-1	H_{comb}	0.1182 / 0.0562	0.5696 / 0.1314	0.6503 / 0.1078	0.7801 / 0.1310	0.8364 / 0.0725
	H_C	0.8880 / 0.0802	0.1028 / 0.0615	0.4080 / 0.1317	0.6931 / 0.1759	0.7128 / 0.1135
	H_J	**0.8262** / 0.0948	**0.2799** / 0.1410	0.7535 / 0.1462	0.8330 / 0.1450	0.9234 / 0.0575
	H_L	0.9270 / 0.0568	0.1732 / 0.0967	**0.5860** / 0.1534	**0.8160** / 0.1561	**0.8747** / 0.0819

The boldface values serve to emphasize key results. Specifically, the boldface numbers indicate the optimal results among the different methods presented.

Sentinel-1 data exhibit characteristics similar to those of the Gaofen-3 and Radarsat-2 data. Performances of these real DP entropies on sample areas A-E are shown in Fig. 6(c), where the H_{comb} for reference is obtained by combining the H of Gaofen-3 and Radarsat-2 data. As shown in Fig. 6, the specific values of which are listed in Table III, the phenomenon that $H_C \leq H_L \leq H_J$ can be observed for almost all the sample areas of the three data, except for the Radarsat-2 data of area D, the H_L of which is slightly larger than H_J, and for the Sentinel-1 data of area A, all the DP entropies deviate significantly from H_{comb}. On areas C, D, and E, results from the three data are highly consistent, with H_L performing better than H_C and H_J, demonstrating good agreement with the target FP entropy.

On areas A and B, results from the measured DP data not only differ from the FP entropy H but also vary from those of the simulated data. This discrepancy may be attributed to two factors. First, the lack of information regarding S_{HH} makes the difference between the DP and FP entropies inevitable. The impact of S_{HH} on DP entropy estimation, as shown in Fig. 1(d)–(f), is challenging to predict. For instance, the H_L of area B is underestimated due to the small S_{VH} component of the target, and the existence of S_{HH} will increase the degree

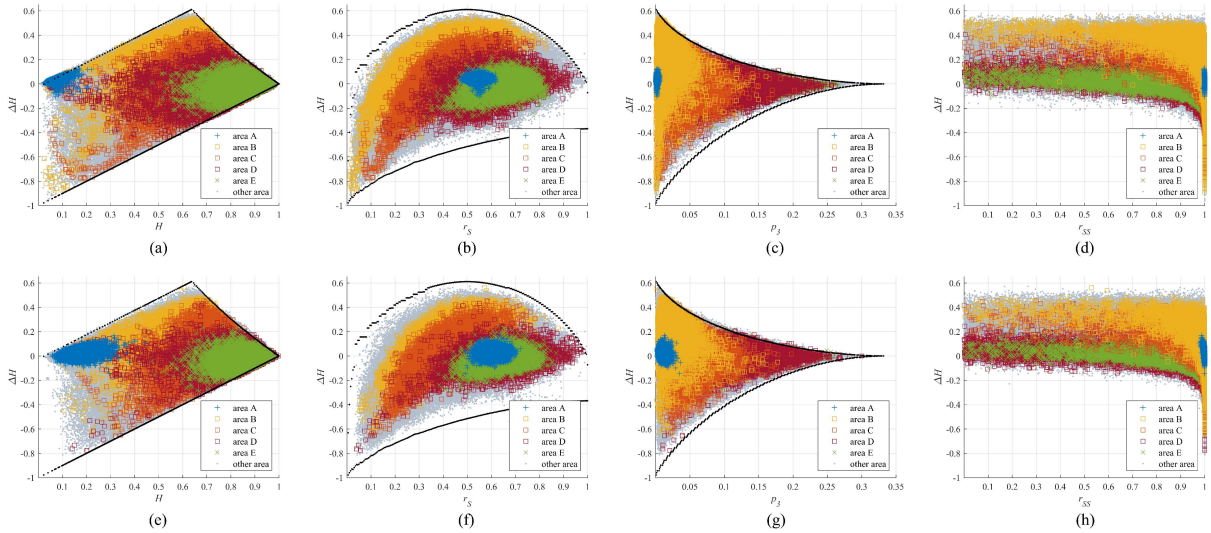

Fig. 9. Relationships between ΔH and its influencing parameters (a) and (e) H, (b) and (f) r_S, (c) and (g) p_3, and (d) and (h) r_{SS}. Images of the first and second rows are the results of the Gaofen-3 and Radarsat-2 data, respectively. The black dotted lines in (a)–(c) and (e)–(g) depict boundaries given by theoretical analysis.

of randomness. Conversely, the H_L of area E is overestimated because of the high S_{VH} component, which can be moderated to the level of H by including S_{HH}. Second, it is known that the DP SAR measurements are not equivalent to the FP ones in several aspects, including calibration. Thus, the ideal estimation provided by simulated data cannot be obtained in practice, and the difference of DP entropies on area B between Fig. 6(a)–(c) is reasonable. As for the ocean area A, due to the large incident angle of Sentinel-1, which results in the small radar cross-section, the measurement deviation may be more pronounced than in other target areas.

The experiment demonstrates strong consistency between the measured and the simulated DP data in estimating entropy for medium and high randomness targets, and when compared to H_C and H_J, H_L proves to be a more accurate substitute for H. These findings are in line with the theoretical analysis presented in Section III, which suggests that as the FP entropy of the target increases, the gap between DP and FP entropies decreases. In addition, experimental results based on Sentinel-1 data also show the poor abilities of H_C and H_J for distinguishing different targets, as H_C is usually larger than H and H_J is usually smaller than H, which is in conformity with the classification results in the proceeding subsection. Moreover, this will fundamentally affect their change detection performances, which will be further analyzed in Section VI.

D. Discussion on the Difference Between H and H_L

While H_L exhibits greater consistency with H and better target classification performance in comparison to H_C and H_J, we have stressed that the discrepancy between H_L and H (represented by $\Delta H = H - H_L$) is inevitable due to the lack of information about S_{HH}. Building upon the theory presented in Section III-B, the following experiment delves into the factors that significantly influence ΔH and discusses them on different targets marked in Fig. 3.

According to (19)–(23), we identify three parameters that are directly associated with ΔH, i.e., H, r_S, and $1 - p_1 - p_2$ (hereinafter referred to as p_3). Fig. 9(a)–(c) and (e)–(g) illustrate their respective relationships with ΔH based on the Gaofen-3 and Radarsat-2 data, and the black dotted lines represent theoretically derived boundaries. The results for H align with the theoretical analysis for Fig. 1(d). Specifically, when H is less than 0.6309, H_L can take any value between [0, 1], while when H exceeds 0.6309, the range of ΔH decreases with the increase of H. The effect of r_S on ΔH is predictable at both ends of its range. For very small r_S values ($r_S \leq 0.1$), indicating that target DP power is small compared to its FP power, most of the polarimetric information is associated with S_{HH}, so H is small and H_L can assume any value within the [0, 1] range. When r_S equals 1, denoting targets with no S_{HH}-related information, it can be deduced that $p_1 = p_L$ and $p_3 = 0$. Consequently, H corresponds to H_L one-to-one, and ΔH varies within the interval $[-0.3691, 0]$, decreasing as H increases. The relationship between p_3 and ΔH is evident; as p_3 increases, the uncertainty of ΔH gradually decreases until it converges to 0. This implies that compared to H and r_S, p_3 is a clearer indicator of the performance of H_L.

In addition to the parameters directly associated with H_L, the relationship between target scattering mechanisms and ΔH is also investigated. In Section III-B, we point out that when H is relatively small, the significant difference between H and H_L may arise from the high correlation between the dominant scattering mechanism of the target and the missing information in DP data. The scattering vector of the target dominant scattering mechanism is the eigenvector $\boldsymbol{u}_1$ corresponding to the maximum eigenvalue λ_1 obtained after the eigendecomposition of $[C]$. While the scattering vector represented by the missing information in the DP data can be approximately constructed as

$$\boldsymbol{k}_{\text{mis}-a} = \left[\sqrt{C_{11}} \quad \frac{C_{12}^*}{\sqrt{C_{11}}} \quad \frac{C_{13}^*}{\sqrt{C_{11}}}\right]^{\text{T}}. \tag{24}$$

Note that we say approximately because the covariance matrix constructed by $\boldsymbol{k}_{\text{mis}-a}$ is

$$[C_{\text{mis}-a}] = \langle \boldsymbol{k}_{\text{mis}-a} \cdot \boldsymbol{k}_{\text{mis}-a}^{*\text{T}} \rangle = \begin{bmatrix} C_{11} & C_{12} & C_{13} \\ C_{12}^{*} & \frac{|C_{12}|^2}{C_{11}} & \frac{C_{12}^{*} C_{13}}{C_{11}} \\ C_{13}^{*} & \frac{C_{12} C_{13}^{*}}{C_{11}} & \frac{|C_{13}|^2}{C_{11}} \end{bmatrix} \tag{25}$$

while the actual covariance matrix of the DP missing information is

$$[C_{\text{mis}}] = \begin{bmatrix} C_{11} & C_{12} & C_{13} \\ C_{12}^{*} & 0 & 0 \\ C_{13}^{*} & 0 & 0 \end{bmatrix}. \tag{26}$$

Nonetheless, as $[C_{\text{mis}-a}]_{(2,2)}$ and $[C_{\text{mis}-a}]_{(3,3)}$ are relatively small compared to $[C_{\text{mis}-a}]_{(1,1)}$, the difference between them has little impact on the analysis. More importantly, since $[C_{\text{mis}}]$ cannot be the covariance matrix of a real target unless $C_{12} = C_{13} = 0$ [43], [44], the approximation is necessary. The correlation between $\boldsymbol{k}_{\text{mis}-a}$ and $\boldsymbol{u}_1$ can be evaluated using the polarimetric scattering similarity [45], calculated as

$$r_{SS} = \frac{\boldsymbol{k}_{\text{mis}-a}^{*\text{T}} \cdot \boldsymbol{u}_1 \cdot \boldsymbol{u}_1^{*\text{T}} \cdot \boldsymbol{k}_{\text{mis}-a}}{\text{Tr}\left(\boldsymbol{k}_{\text{mis}-a} \cdot \boldsymbol{k}_{\text{mis}-a}^{*\text{T}}\right) \cdot \text{Tr}\left(\boldsymbol{u}_1 \cdot \boldsymbol{u}_1^{*\text{T}}\right)} \tag{27}$$

where $\text{Tr}(\cdot)$ is the trace operation of a matrix, and $r_{SS} \in [0, 1]$. Fig. 9(d) and (h) respectively present the relationship between r_{SS} and ΔH based on the Gaofen-3 and Radarsat-2 data. It can be observed that when there is no apparent correlation between the two, the distribution of ΔH is relatively uniform, ranging between -0.1 and 0.5. On the other hand, a strong correlation between the two ($r_{SS} \geq 0.8$) corresponds to the situation where H and H_L exhibit the greatest differences in values. For instance, for targets with $\Delta H \leq -0.4$, there always exists $r_{SS} = 1$.

We also mark the targets of sample areas A-E in Fig. 9. It can be observed that mountainous area E, characterized by high H and high p_3 values, r_S between 0.4 and 0.8, and low r_{SS} value, exhibits a relatively small ΔH. Urban areas B, C, and D display similar ΔH characteristics, with ΔH gradually decreasing as H increases due to the orientation effect. Images of r_{SS} reveal a significant correlation between the primary scattering mechanism of urban targets and the polarimetric information missing in the simulated DP model, especially evident in the low-entropy area B. This explains the substantial difference in H_L and H observed in region B of Fig. 6. For ocean area A, ΔH is relatively small based on simulated data, yet its r_{SS} is close to 1, indicating a high correlation between its $\boldsymbol{k}_{\text{mis}-\boldsymbol{a}}$ and $\boldsymbol{u}_1$. Consequently, although the simulated situation results in nearly equal DP and FP entropies for the ocean, significant ΔH values may occur in actual measured data, as demonstrated by the Sentinel-1 data shown in Fig. 4.

The analysis of factors influencing ΔH leads to the conclusion that H_L serves as an excellent surrogate for H in targets with medium to high entropy or large p_3 values. However, for targets with low entropy, the performance of H_L is related to r_{SS}. Taking the polarimetric mode of Sentinel-1 as an example, urban areas and the ocean may exhibit significant inconsistencies between H_L and H due to their extremely high r_{SS} values.

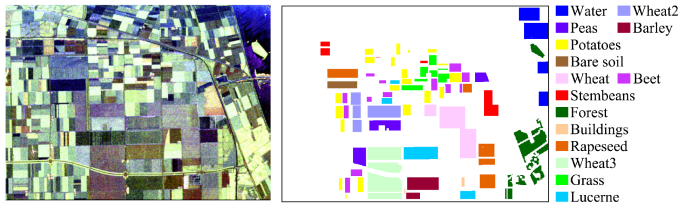

Fig. 10. Images of the experimental area in Flevoland, Netherlands, where (a) is the Pauli vector color-coded image and (b) is the ground truth map with a total of 15 types of targets identified.

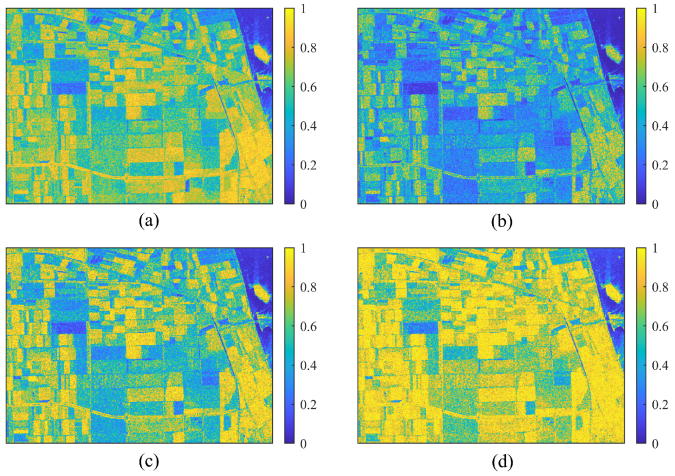

Fig. 11. FP and DP entropies derived from the Flevoland data, i.e., (a) H, (b) H_C, (c) H_L, and (d) H_J.

V. Experiment With AIRSAR L-Band FP Data From Flevoland

It is noted that although the preceding section conducted a comprehensive study of different entropies, the San Francisco data used only contain two types of low-to-medium entropy ($H < 0.6$) targets, i.e., ocean and small POA urban area. Research by Cloude and Pottier has indicated that the scattering characteristics related to $H < 0.6$, in addition to the Bragg surface and dihedral reflector, also include volume diffusion (dipole or anisotropic particles), random surface, etc. [11], [12]. Therefore, this section supplements an analysis of the AIRSAR L-Band FP data acquired in Flevoland, Netherlands, which predominantly includes agricultural crops with the above scattering types.

The RGB image of the experimental area coded by Pauli vector [1] is shown in Fig. 10(a), and (b) is the corresponding ground truth map with a total of 15 types of targets identified [46], i.e., water, three kinds of wheat, peas, barely, potatoes, bare soil, beet, stem beans, forest, buildings, rapeseed, grass, and lucerne. Fig. 11(a) shows the derived FP entropy H, from which it can be seen that there are a large number of low and medium entropy targets, and the calculated proportion of targets with $H < 0.6$ is

TABLE IV
STATISTICAL DIFFERENCES BETWEEN FP ENTROPY AND DP ENTROPIES ON AIRSAR DATA FROM FLEVOLAND

Class	MAD / RMSD (/ R^2)		
	H_C	H_J	H_L
Overall	0.1906 / 0.2159 / -0.1743	0.1404 / 0.1665 / 0.3017	**0.0846 / 0.1089 / 0.7009**
Water	0.0646 / 0.0755	0.0385 / 0.0498	**0.0307 / 0.0400**
Wheat 2	0.2450 / 0.2518	**0.0776 / 0.0948**	0.1163 / 0.1303
Peas	0.1944 / 0.2051	0.1850 / 0.1998	**0.0617 / 0.0770**
Barley	0.2492 / 0.2623	0.1277 / 0.1454	**0.0806 / 0.0944**
Potatoes	0.1233 / 0.1451	0.1402 / 0.1600	**0.0779 / 0.0960**
Bare soil	0.1338 / 0.1393	0.0624 / 0.0780	**0.0611 / 0.0702**
Wheat	0.2775 / 0.2852	**0.0855 / 0.1040**	0.1214 / 0.1383
Beet	0.1444 / 0.1627	0.1993 / 0.2128	**0.0790 / 0.0972**
Stem beans	0.2381 / 0.2636	0.1258 / 0.1479	**0.1064 / 0.1321**
Forest	0.1654 / 0.1870	0.0666 / 0.0811	**0.0492 / 0.0634**
Buildings	**0.1685 / 0.1899**	0.4780 / 0.5054	0.3157 / 0.3431
Rapeseed	0.1965 / 0.2063	0.1645 / 0.1799	**0.0614 / 0.0777**
Wheat 3	0.3361 / 0.3430	**0.0683 / 0.0849**	0.1824 / 0.1972
Grass	0.2332 / 0.2491	0.1503 / 0.1719	**0.0865 / 0.1071**
Lucerne	0.2801 / 0.3028	**0.0981 / 0.1195**	0.1226 / 0.1501

The boldface values serve to emphasize key results. Specifically, the boldface numbers indicate the optimal results among the different methods presented.

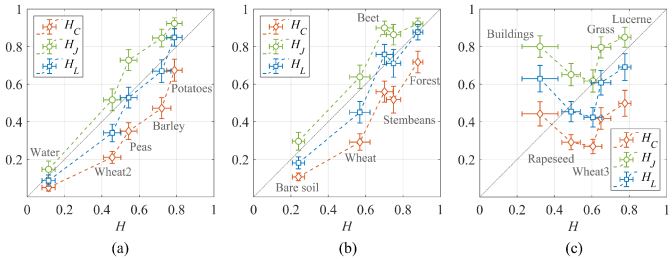

Fig. 12. Relationships between H and DP entropies on different kinds of targets, i.e., (a) water, wheat2, peas, barley, potatoes, (b) bare soil, wheat, stembeans, beet, forest, (c) buildings, rapeseed, wheat3, grass, and lucerne, from the Flevoland data, presented in three groups for clarity.

42.45%. DP entropies in this section are derived from the data extracted with the same polarization mode of Sentinel-1 (i.e., VV-VH). As shown in Fig. 11(b)–(d), they exhibit characteristics consistent with the preceding experiment, i.e., H_L has better consistency with H, and H_C appears smaller while H_J appears larger than H. This observation can be corroborated by the MAD, RMSD, and R^2 values of different DP entropies calculated with H as the reference value (Row 3 of Table IV). Since the histogram of the difference between H and DP entropies of this data is highly similar to the previous experimental results, it is not shown again.

A comparative analysis of different DP entropies is conducted based on the 15 types of targets marked in Fig. 10(b). Fig. 12 illustrates the relationships between FP and DP entropies across different targets, presented in three groups for clarity, and the corresponding summary statistics are displayed as box charts in Fig. 13. The distinct feature of $H_C \leq H_L \leq H_J$ indicates the data characteristic of $r_C \geq \sqrt{2}$, and the specific values can be found in Table V. The statistical features of the difference between H and DP entropies of the 15 types of targets are shown in Table IV. It is evident that for most categories of targets, H_L has better consistency with H, which results in its significant advantage in MAD, RMSD, and R^2 for the overall data. Exceptions are noted in Buildings, the three wheat categories, and lucerne. In addition, although the mean of H_J (0.2962) for bare soil is closer to the mean of H (0.2403) than that of H_L (0.1812), Fig. 12(b) indicates minimal performance difference between H_J and H_L, and Table IV reflects the superiority of H_L in MAD and RMSD. It has been discussed that the scattering mechanism of buildings will cause a large difference between H and DP entropies, as shown in Fig. 9(d) and (h). Moreover, due to the small sample size [see Fig. 10(b)] and the dispersed distribution of H [see Fig. 13(a)], it is reasonable to observe the inferior performance of DP entropies. The means of H_L and H_C of the three types of wheat and lucerne are all less than that of H. As can be known from the previous analysis of the parameters affecting ΔH, this is due to the high correlation between the target scattering mechanism and the missing information. The calculated proportions of $r_{SS} > 0.8$ in wheat, wheat2, wheat3, and lucerne are 83.11%, 97.80%, 61.51%, and 79.30%, respectively. On the other hand, the better performance of H_J for lucerne may also attributed to its advantage in estimating high entropy targets, since the mean of H of the lucerne is as high as 0.7759.

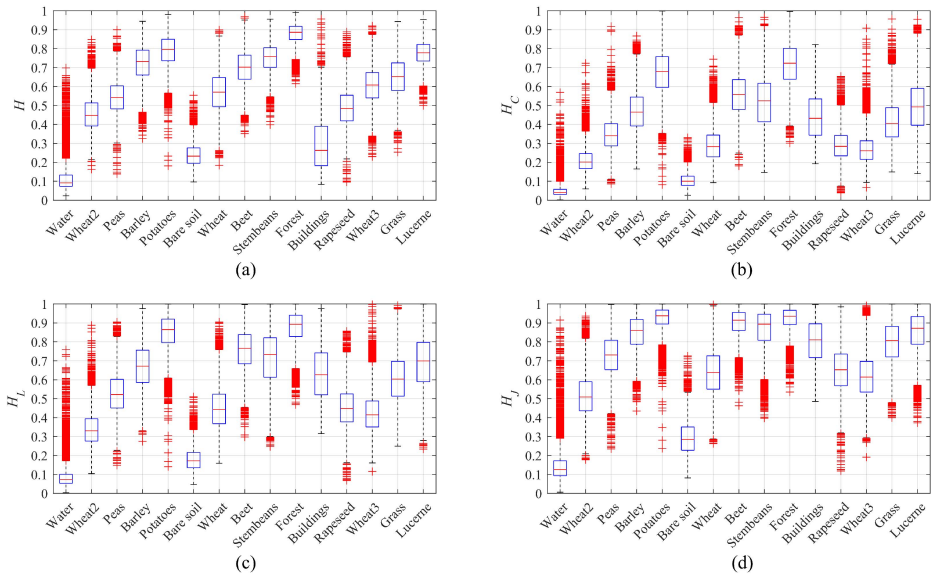

Fig. 13. Box charts of (a) FP entropy H and DP entropies (b) H_C, (c) H_L, and (d) H_J across different targets from the Flevoland data.

TABLE V
STATISTICAL CHARACTERISTICS OF DIFFERENT ENTROPIES IN DIFFERENT CLASSES OF AIRSAR FLEVOLAND DATA

Class	Mean / Standard Deviation			
	H	H_C	H_J	H_L
Water	0.1146 / 0.0701	0.0500 / 0.0376	0.1470 / 0.0886	**0.0869** / 0.0596
Wheat 2	0.4556 / 0.0920	0.2106 / 0.0647	**0.5165** / 0.1157	0.3405 / 0.0927
Peas	0.5437 / 0.0902	0.3500 / 0.0891	0.7278 / 0.1115	**0.5289** / 0.1104
Barley	0.7208 / 0.0975	0.4717 / 0.1115	0.8456 / 0.0943	**0.6696** / 0.1202
Potatoes	0.7884 / 0.0831	0.6745 / 0.1182	0.9234 / 0.0599	**0.8492** / 0.0934
Bare soil	0.2403 / 0.0651	0.1066 / 0.0405	**0.2962** / 0.0943	0.1812 / 0.0642
Wheat	0.5692 / 0.1091	0.2917 / 0.0870	**0.6388** / 0.1253	0.4505 / 0.1147
Beet	0.7008 / 0.0913	0.5599 / 0.1122	0.8998 / 0.0709	**0.7582** / 0.1073
Stem beans	0.7495 / 0.0767	0.5178 / 0.1429	0.8636 / 0.1090	**0.7112** / 0.1471
Forest	0.8799 / 0.0529	0.7177 / 0.1146	0.9216 / 0.0601	**0.8770** / 0.0821
Buildings	0.3221 / 0.1924	**0.4421** / 0.1294	0.7999 / 0.1143	0.6292 / 0.1409
Rapeseed	0.4884 / 0.0983	0.2919 / 0.0801	0.6510 / 0.1189	**0.4541** / 0.1070
Wheat 3	0.6055 / 0.0954	0.2694 / 0.0762	**0.6169** / 0.1175	0.4236 / 0.1032
Grass	0.6490 / 0.1042	0.4174 / 0.1155	0.7956 / 0.1122	**0.6077** / 0.1308
Lucerne	0.7759 / 0.0652	0.4984 / 0.1382	**0.8496** / 0.1062	0.6911 / 0.1423

The boldface values serve to emphasize key results. Specifically, the boldface numbers indicate the optimal results among the different methods presented.

It is important to note that while the aforementioned performance of H_L on low-to-medium entropy targets is intrinsically related to the scattering characteristics of the targets, it can also be predicted theoretically by the relationship between H_L and H derived in Section III. Specifically, when H is less than 0.6309, the range of H_L is [0, 1], making it more likely to exhibit a greater deviation from H compared to medium-to-high entropy targets. On the other hand, since the ranges of H_C and H_J for low-to-medium entropy targets are also [0, 1], there is also no definitive conclusion that H_C or H_J performs better than H_L on such targets, as demonstrated by the experimental results: H_L always maintains optimal or suboptimal results. Furthermore, as illustrated by the box charts, it distinguishes different targets more effectively than H_C and H_J, i.e., the values of H_C are usually smaller and generally distributed in the low- and medium-entropy zone, while the values of H_J are usually larger and generally distributed in the medium- and high-entropy zone. In summary, the experimental results based on the crop

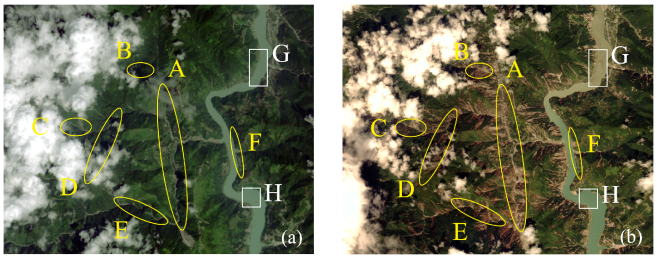

Fig. 14. Optical images of the experimental area in Wandong Village of Luding County obtained (a) before and (b) after the earthquake, respectively. Large landslide areas A–F are marked with yellow ellipses.

data set further demonstrate the superior performance of H_L in both fitting the FP entropy and characterizing the randomness of target scattering.

VI. Landslide Detection in 2022 Luding Earthquake Area Based on Sentinel-1 Data

As previously discussed, DP SAR data have consistently served as a crucial resource in the domain of environmental monitoring. In this section, an experiment for landslide detection based on DP entropies is conducted to study their change detection performances.

On September 5, 2022, an earthquake with a magnitude of 6.7 struck Luding County in Sichuan Province, China. Since the epicenter is located within the Hengduan Mountains, severe landslides occurred and even dammed a tributary of the Dadu River [28]. Therefore, obtaining environmental information and monitoring its change in time is crucial for early warning of other large-scale geological or secondary disasters that may be further triggered. Considering the rainy and cloudy weather after the earthquake, the DP SAR data of Luding County acquired routinely by Sentinel-1 before (on August 26) and after (on September 7) the disaster is of significant value. Therefore, these two sets of DP data are used in this experiment.

Multiple landslides near the epicenter (29.49 °N, 102.22 °E) were triggered by the earthquake, mainly on the west bank of the Dadu River. Accordingly, the Wandong Village (located at 29.53 °N and 102.15 °E) with dense landslides around is selected as the experimental area, and its optical images before and after the disaster are shown in Fig. 14, which were acquired by Landsat-8 on August 26 and by Gaofen-6 on September 10, respectively. Several large landslides are marked with yellow ellipses, which can be visually identified from the optical images and verified by the postearthquake field photos [47], [48].

Fig. 15(a), (b), (e), (f), (i), and (j) display H_C (the first row), H_J (the second row), and H_L (the third row) derived from the Sentinel-1 DP data acquired before and after the earthquake on August 26 (the first column) and September 7 (the second column), respectively. Since most of the scene are mountains covered by vegetation, entropies are high in all the subfigures, while the phenomenon that generally $H_C \leq H_L \leq H_J$ can still be observed. Taking Fig. 14 as a reference, we can find that entropies of landslide areas decrease sharply compared with the nonlandslide areas, which can be explained by the change of the scattering mechanisms. Specifically, landslides washed away the vegetation and left only the bare surface of the mountain, changing the scattering mechanism from high-entropy volume scattering to low-entropy surface scattering. In order to show the change explicitly, differences between the preearthquake and the postearthquake H_C, H_J, and H_L, namely ΔH_C, ΔH_J, and ΔH_L, are calculated and shown in Fig. 15(c), (g), and (k), respectively, from which some changes can be visually identified despite the noisy points all over. Among the results, ΔH_C fluctuates the most, ΔH_J is the opposite, and ΔH_L is in between. Nevertheless, obvious changes displayed by ΔH_J are much less than that by ΔH_C and ΔH_L, which may be due to its high value thus low object discrimination capability, as analyzed in the preceding section. Note that the entropy of Dadu River also changes significantly, which will be discussed in detail later.

Furthermore, the expectation-maximization (EM) algorithm, which is commonly used for unsupervised change detection [16], [50], is applied to ΔH_C, ΔH_J, and ΔH_L to classify them into increased, unchanged, and decreased categories, respectively. Thus, the landslides can be automatically detected as the entropy decreased category. Fig. 15(d), (h), and (l) show the classification results imposed on the grayscale SPAN image, where yellow and green colors represent classes of entropy decreased and increased, respectively. It can be seen that ΔH_C, ΔH_J, and ΔH_L can detect landslides in areas A, D, E, and F. However, the detected area of ΔH_J is much less than that of ΔH_C and ΔH_L, resulting in reduced detection capability, e.g., changes in areas B and C are not detected (only a few discrete points). On the other hand, the result of ΔH_C seems heavily influenced by random noisy points. Although it has similar detection results with ΔH_L in areas A–F, these points severely confuse the determination of landslides. By contrast, the result of ΔH_L shows its superiority in identifying the landslides A–F effectively and clearly.

To quantitatively compare the landslide detection performance of different entropies, we manually select six landslide areas (ls1-ls6) and three nonlandslide areas (nls1-nls3) based on the true landslide map and correspondingly mark them on the SPAN image, as shown in Fig. 16. It should be noted that due to the large incident angles of Sentinel-1 (40.04°–46.00° for the employed data at Interferometric Wide swath mode beam 3) and the steep terrain of the experimental area, the phenomena of foreshortening and shadow in SAR images are significantly severe. Consequently, the entropy estimation results from the terrain-corrected data are markedly affected by interpolation, making effective change detection unfeasible. Thus, the evaluation is conducted based on the slant range images, as done by related research [15]. The landslide areas are marked on the side of the mountain facing the radar line of sight, which due to the foreshortening effect, appear as narrower strips, reducing the uncertainty in marking landslide areas in the slant range image. The detection results of the three DP entropies are shown in Table VI. It is observed that for all landslide areas except area ls4, the detection accuracy follows the order $H_L > H_C > H_J$, while in area ls4, the accuracy of H_C is slightly higher than H_L. Conversely, for nonlandslide areas, the accuracy order is reversed, i.e., $H_J > H_L > H_C$. This result is consistent with the experimental findings in Sections IV and V. Specifically, since H_C and H_J have lower capabilities in discriminating different targets, indicated by lower kappa coefficients in Table II, their

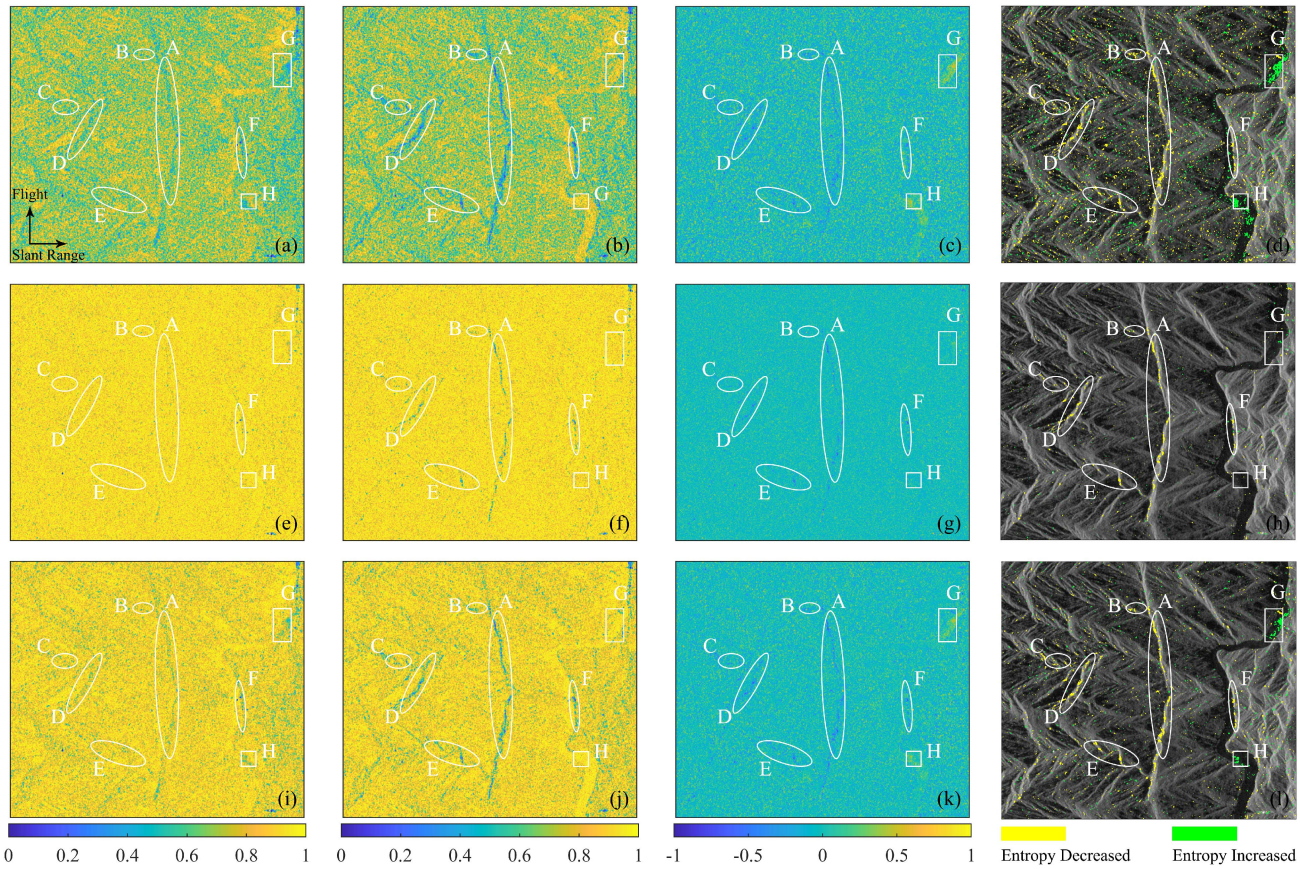

Fig. 15. Images of the experimental area in Wandong Village of Luding County. Results derived from (a)–(d) H_C, (e)–(h) H_J, and (i)–(l) H_L are shown in the first, second, and third rows, respectively. Each column from left to right represents the DP entropy H_t $(t = C, J, L)$ before and after the earthquake, the entropy difference ΔH_t $(t = C, J, L)$, and the change detection result of the ΔH_t $(t = C, J, L)$, respectively.

TABLE VI
DETECTION ACCURACIES (%) OF DIFFERENT DP ENTROPIES IN LANDSLIDE AND NONLANDSLIDE SAMPLE AREAS OF LUDING COUNTY

DP Entropy	ls1	ls2	ls3	ls4	ls5	ls6	nls1	nls2	nls3
H_C	78.26	36.64	42.79	**38.82**	31.72	33.90	94.19	93.37	94.18
H_J	80.43	36.41	25.76	26.89	20.80	34.32	**99.46**	**100**	**99.89**
H_L	**91.30**	**41.13**	**44.54**	38.15	**33.28**	**40.25**	98.50	96.19	98.31

The boldface values serve to emphasize key results. Specifically, the boldface numbers indicate the optimal results among the different methods presented.

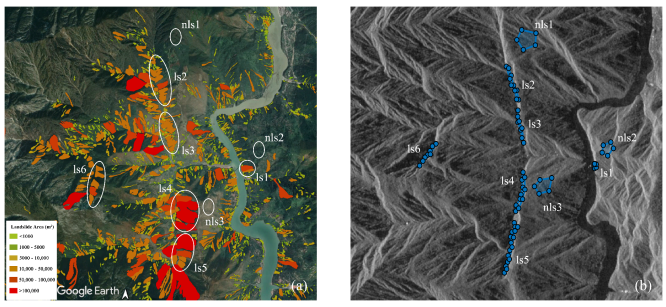

Fig. 16. Images of the experimental area with manually determined regions of interest, i.e., (a) optical landslide map [49] and (b) SPAN image with six landslide areas (ls1-ls6) and three nonlandslide areas (nls1-nls3) marked.

abilities to distinguish between low-entropy surface scattering and high-entropy volume scattering are weaker than H_L, resulting in lower landslide detection accuracy compared to H_L. On the other hand, since H_C usually has a lower value and H_J usually has a higher value, ΔH_C fluctuates more and ΔH_J has a smaller dynamic range. Accordingly, it is reasonable for H_C to achieve higher landslide detection accuracy than H_J, and thus, instances where it exceeds H_L can be considered plausible. At the same time, the low accuracy of H_C for nonlandslide detection is inevitable. And H_J will have higher accuracy for nonlandslide detection than H_C and H_L, although their differences are quite small. It is noted that apart from ls1, the detection accuracies in other landslide areas are not high, which may be attributed to the influence of the mountainous terrain fluctuations

and the low resolution of Sentinel-1 data, both affecting the entropy estimation. However, for area ls1 with a small thus relatively flat surface,where boundaries can be clearly discerned, all three DP entropies perform well, and the results of H_C are close to the experimental results in [15] (0.85). In summary, the experimental results demonstrate the superiority of H_L in landslide detection compared to existing DP entropies. This can be ultimately attributed to its more accurate description of the polarimetric randomness of target scattering, as illustrated by the aforementioned theory analysis and comparative experiments.

The state of the Dadu River is also worth mentioning. As its entropy [see Fig. 15(a), (b), (e), (f), (i), and (j)] shows a similar characteristic to the water bodies shown in Fig. 4(i), (j), and (k), it indicates that estimating entropy for water bodies based on Sentinel-1 data is unreliable. However, it is shown in Fig. 15(c) and (k) that entropies of areas G and H increase after the earthquake. This is reasonable given that they are both river bends and close to areas of landslides and mudslides triggered by the earthquake and subsequent rainfall, i.e., rocks, sand, and other kinds of sediments have entered the river, increasing the randomness of the polarimetric scattering. The inference can be supported by filed photos of other parts of Dadu River and the formation of a dammed lake after the earthquake [47], [48], [51]. However, the entropy change of the river cannot be detected by ΔH_J.

VII. Discussion

Polarimetric entropy, as an indispensable parameter extracted from FP SAR data, reflects the polarimetric randomness of target scattering and has been widely used in applications such as land cover classification, target recognition, and disaster detection. Compared to existing DP entropies, the new DP entropy proposed in this article not only improves the ability to extract target features, providing better discrimination among different targets, but also achieves highly consistent estimation results with the target FP entropy under conditions of limited polarization information. Several points regarding this work are further discussed below.

Reciprocity is the theoretical basis of this work, and here we delve into it from its influencing factors and correction methods. It has been concluded by Cameron and Leung [32] that *if reciprocity is violated it is likely to be due to propagation effects, interaction with special materials (materials whose interaction with the electromagnetic field is nonlinear or which are described by dielectric, permeability or conductivity tensors which are asymmetric) or, for low RCS returns, perhaps measurement noise*. It is known that the propagation effects, such as Faraday rotation, need to be corrected through Faraday rotation compensation, while nonreciprocal materials are not common in natural surface observations, and research on them should be carried out totally based on their asymmetric scattering matrices. Accordingly, Cameron and Leung [32] propose a method for extracting the reciprocity component of the target that primarily aims at correcting measurement errors, the form of which is essentially equivalent to (3). Similarly, it has also been discussed in a document for calibrating the ALOS PALSAR products that [52], *symmetrization is an optional step that forces to be equal the cross-polarized channels in presence of system noise*. And the provided correction method also has the same form of (3) when there is no *receive to transmit channel imbalance* [52]. According to the above analysis, it can be seen that from the perspective of theoretical analysis, (3) represents the ideal cross-polarization component of a reciprocal target satisfying $S_{HV} = S_{VH}$, and in the sense of practical application, (3) is essentially a reciprocity correction method.

Section V complements Section IV by conducting experiments based on AIRSAR crop data, aiming to enrich the analysis of DP entropy performance for targets with $H < 0.6$. The experimental results are highly consistent with those of Section IV, i.e., although a few targets show large differences between H_L and H, overall, H_L shows distinct advantages over existing DP entropies. Moreover, since the targets with large differences between H_L and H primarily belong to the wheat category, while we analyze the phenomenon based on r_{SS}, future studies could delve deeper into modeling their scattering mechanisms. Furthermore, the ability of a single DP entropy parameter to describe target characteristics is limited, which is also the reason why there is no classification experiment for the Flevoland data. It is believed that in the future, by combining more DP parameters and using more advanced methods [46], [53], [54], [55], the advantages of H_L can be more fully utilized.

It is worth noting that although we apply the proposed theory to the DP data of Sentinel-1, the theoretical analysis approach is generally applicable to other DP modes. However, the performance of the DP entropy on various targets needs further investigation, as the polarimetric information of the target contained in DP data has changed at this time. Besides, for cases where the reciprocity theorem does not hold, the rigorous entropy estimation method proposed by Cloude may be a better choice, and the FP entropy that represents the true target polarimetric randomness in such situations should be derived from a 4×4 covariance matrix [1].

VIII. Conclusion

This article studies the method of polarimetric entropy estimation from DP SAR data and proposes a new entropy estimation method based on the reciprocity assumption, which improves the performance of DP entropy in depicting target polarimetric characteristics and fills the gaps in its theoretical research. Since the reciprocity theorem holds in the vast majority of natural terrain remote sensing using monostatic backscatter SAR, the proposed method is generally applicable, as demonstrated by the comparative experiment of the article. The proposed method is not only physically meaningful but also establishes a mathematical connection with the FP entropy H. Accordingly, it also completes the theoretical research on existing DP entropies H_C and H_J. Theoretical analysis shows that compared to H_C and H_J, the newly estimated DP entropy H_L has higher consistency with H and can more accurately reflect the polarimetric characteristics of the target. Experiments based on multisource San Francisco polarimetric SAR data validate the theory and demonstrate the superiority of H_L in target classification, with higher overall accuracy and kappa coefficient, while H_C and H_J respectively show advantages in low and high entropy targets. Nonetheless, the experiment based on Flevoland data implies that on various

crops, nearly half of which with low-to-medium entropy, H_L still maintains an absolute advantage in reflecting the target randomness. In addition, its temporal difference ΔH_L has a higher landslide detection accuracy, with a lower noise level compared to ΔH_C and a higher change detection ability compared to ΔH_J. Besides, factors affecting the difference between H and H_L are also theoretically analyzed and experimentally illustrated, clarifying their similarity on medium- and high-entropy targets and potential divergence on low-entropy targets and providing guidance for applying H_L as a substitute for H.

Appendix A

This appendix introduces the calculation methods of DP entropies H_C, H_J, and H_L in detail as a supplement to (10)–(15) in the article.

According to the definition [7], [8], [12], DP entropy is calculated by

$$\begin{aligned} H_D &= -\sum_{k=1}^{2} p_{D_k} \log_2(p_{D_k}) \\ &= -p_{D_1} \log_2(p_{D_1}) - p_{D_2} \log_2(p_{D_2}) \end{aligned} \tag{28}$$

where

$$p_{D_k} = \frac{\lambda_{D_k}}{\sum_{m=1}^{2} \lambda_{D_m}} \qquad (k = 1, 2) \tag{29}$$

and λ_{D_k} $(k = 1, 2)$ are the eigenvalues of the DP covariance matrix with $\lambda_{D_1} \geq \lambda_{D_2}$ without loss of generality. Since $p_{D_1} + p_{D_2} = 1$ [according to (29)], we can simplify the representation in (28) using only p_{D_1}, the maximum pseudoprobability, as

$$H_D = -p_{D_1} \log_2(p_{D_1}) - (1 - p_{D_1}) \log_2(1 - p_{D_1}) \tag{30}$$

which has the same form as (10).

According to (30), the maximum pseudoprobability p_{D_1} uniquely determines the DP entropy H_D, while itself is derived from the DP covariance matrix. Cloude [7], Ji and Wu [8], and this article construct the DP covariance matrices $[C_C]$, $[C_J]$, and $[C_L]$, respectively, as

$$[C_C] = \langle \boldsymbol{c}_C \cdot \boldsymbol{c}_C^{*\mathrm{T}} \rangle = \left\langle \begin{bmatrix} |S_{VV}|^2 & S_{VV} S_{VH}^* \\ S_{VH} S_{VV}^* & |S_{VH}|^2 \end{bmatrix} \right\rangle \tag{31}$$

$$[C_J] = \langle \boldsymbol{c}_J \cdot \boldsymbol{c}_J^{*\mathrm{T}} \rangle = \left\langle \begin{bmatrix} |S_{VV}|^2 & 2S_{VV} S_{VH}^* \\ 2S_{VH} S_{VV}^* & 4|S_{VH}|^2 \end{bmatrix} \right\rangle \tag{32}$$

$$[C_L] = \langle \boldsymbol{c}_L \cdot \boldsymbol{c}_L^{*\mathrm{T}} \rangle = \left\langle \begin{bmatrix} |S_{VV}|^2 & \sqrt{2} S_{VV} S_{VH}^* \\ \sqrt{2} S_{VH} S_{VV}^* & 2|S_{VH}|^2 \end{bmatrix} \right\rangle \tag{33}$$

and the maximum eigenvalue λ_t $(t = C, J, L)$ of the 2×2 Hermitian covariance matrix $[C_t]$ $(t = C, J, L)$ can be solved analytically, as

$$\lambda_C = \frac{1}{2} \left(\langle |S_{VV}|^2 \rangle + \langle |S_{VH}|^2 \rangle + \sqrt{(\langle |S_{VV}|^2 \rangle - \langle |S_{VH}|^2 \rangle)^2 + 4 |\langle S_{VV} S_{VH}^* \rangle|^2} \right) \tag{34}$$

$$\lambda_J = \frac{1}{2} \left(\langle |S_{VV}|^2 \rangle + \langle 4 |S_{VH}|^2 \rangle + \sqrt{(\langle |S_{VV}|^2 \rangle - \langle 4 |S_{VH}|^2 \rangle)^2 + 4 |\langle 2 S_{VV} S_{VH}^* \rangle|^2} \right) \tag{35}$$

$$\lambda_L = \frac{1}{2} \left(\langle |S_{VV}|^2 \rangle + \langle 2 |S_{VH}|^2 \rangle + \sqrt{(\langle |S_{VV}|^2 \rangle - \langle 2 |S_{VH}|^2 \rangle)^2 + 4 |\langle \sqrt{2} S_{VV} S_{VH}^* \rangle|^2} \right). \tag{36}$$

Then, the corresponding maximum pseudoprobabilities p_C, p_J, and p_L can be derived according to (29), as

$$p_C = \frac{1}{2} + \frac{\sqrt{(\langle |S_{VV}|^2 \rangle - \langle |S_{VH}|^2 \rangle)^2 + 4 |\langle S_{VV} S_{VH}^* \rangle|^2}}{2 (\langle |S_{VV}|^2 \rangle + \langle |S_{VH}|^2 \rangle)} \tag{37}$$

$$p_J = \frac{1}{2} + \frac{\sqrt{(\langle |S_{VV}|^2 \rangle - \langle 4 |S_{VH}|^2 \rangle)^2 + 4 |\langle 2 S_{VV} S_{VH}^* \rangle|^2}}{2 (\langle |S_{VV}|^2 \rangle + \langle 4 |S_{VH}|^2 \rangle)} \tag{38}$$

$$p_L = \frac{1}{2} + \frac{\sqrt{(\langle |S_{VV}|^2 \rangle - \langle 2 |S_{VH}|^2 \rangle)^2 + 4 |\langle \sqrt{2} S_{VV} S_{VH}^* \rangle|^2}}{2 (\langle |S_{VV}|^2 \rangle + \langle 2 |S_{VH}|^2 \rangle)}. \tag{39}$$

It can be seen that by substituting r_C and r_X of (15) into (37)–(39), the expressions shown in (12)–(14) can be obtained. Accordingly, DP entropies H_C, H_J, and H_L can be calculated according to p_C, p_J, and p_L using (30), respectively.

Appendix B

This appendix introduces the simulation steps of the relationships between different entropies shown in Fig. 1.

The simulation procedure for illustrating the relationship between DP entropies is as follows:

1) Define values for p_L (ranging from 1/2 to 1, uniformly sampling 128 points) and r_C (ranging from 0 to 60, uniformly sampling 30 000 points), and determine the corresponding r_X values by

$$r_X = \left(p_L - \frac{1}{2} \right)^2 (r_C + 1)^2 - \frac{1}{4} (r_C - 1)^2. \tag{40}$$

   Note that the value of r_C can theoretically be infinite. However, considering its distribution of actual data and the reflection of the DP entropy relationship, taking the maximum value to 60 is sufficient.
2) For each pair of (r_C, r_X), calculate p_C and p_J using (12) and (13).
3) Using (30), compute H_L, H_C, and H_J from p_L, p_C, and p_J, thereby obtaining the relationship graphs for H_L versus H_C and H_L versus H_J, respectively.
4) The relationship graph between H_J and H_C can be derived similarly, by replacing p_L with p_C in step 1) and modifying

the formula for r_X in step 2) to:

$$r_X = 2\left(p_C - \frac{1}{2}\right)^2\left(r_C + \frac{1}{2}\right)^2 - \frac{1}{2}\left(r_C - \frac{1}{2}\right)^2 \tag{41}$$

and all other parameters remain the same.

It should be noted that although step 3) obtains the values of H_C and H_J, it does not establish a relationship between them. This is because the H_C and H_J obtained in step 3) are functions of r_C and r_X, i.e., $H_C = f_C(r_C, r_X)$ and $H_J = f_J(r_C, r_X)$. To establish a relationship between them, we need to solve for $H_J = f_{JC}(H_C)$. In summary, steps 1)-3) derive $H_C = f_{CL}(H_L)$ and $H_J = f_{JL}(H_L)$, while step 4) derives $H_J = f_{JC}(H_C)$.

The simulation procedure for illustrating the relationship between FP entropy H and DP entropies is outlined as follows.

1) Define values for p_1 (ranging from 1/3 to 1, uniformly sampling 128 points) and p_2 (ranging from 0 to 1/2, uniformly sampling 128 points), and determine the corresponding FP entropy H using (5).
2) For each pair of (p_1, p_2), calculate r_S using (22).
3) For each set of (p_1, p_2, r_S), determine the range of p_L using (23).
4) Calculate H_L from p_L, thereby obtaining the relationship graph between H_L and H.
5) Based on the relationship between H_L and H_C (or H_J), derive the relationship graph between H_C (or H_J) and H.

Note that to enhance the aesthetic appeal of the graphs, we performed downsampling on the scatter plots of the relationships obtained, which does not affect the overall shape. The theoretical simulation results are perfectly validated on FP data obtained by Gaofen-3 and Radarsat-2, as shown in Fig. 2, demonstrating the effectiveness of the proposed theory.

ACKNOWLEDGMENT

The authors would like to thank the China National Space Administration (CNSA), the Canadian Space Agency (CSA), the European Space Agency (ESA), and the National Aeronautics and Space Administration (NASA) for providing the outstanding Gaofen-3, Radarsat-2, Sentinel-1, and AIRSAR polarimetric SAR data, respectively. The authors would like to thank the editors and the anonymous reviewers for their valuable comments and suggestions.

REFERENCES

[1] J.-S. Lee and E. Pottier, *Polarimetric Radar Imaging: From Basics to Applications*. Boca Raton, FL, USA: CRC Press, 2009.
[2] S. R. Cloude, *Polarisation: Applications in Remote Sensing*. London, U.K.: Oxford Univ. Press, 2010.
[3] T. Ainsworth, J. Kelly, and J.-S. Lee, "Classification comparisons between dual-pol, compact polarimetric and quad-pol SAR imagery," *ISPRS J. Photogrammetry Remote Sens.*, vol. 64, no. 5, pp. 464–471, 2009.
[4] L. Xie, H. Zhang, C. Wang, and Z. Shan, "Similarity analysis of entropy/alpha decomposition between HH/VV dual-and quad-polarization SAR data," *Remote Sens. Lett.*, vol. 6, no. 3, pp. 228–237, 2015.
[5] W. Wagner, D. Sabel, M. Doubkova, M. Hornáček, S. Schlaffer, and A. Bartsch, "Prospects of Sentinel-1 for land applications," in *Proc. IEEE Int. Geosci. Remote Sens. Symp.*, 2012, pp. 1741–1744.
[6] T. L. Ainsworth, J. Kelly, and J.-S. Lee, "Polarimetric analysis of dual polarimetric SAR imagery," in *Proc. 7th Eur. Conf. Synthetic Aperture Radar*, 2008, pp. 1–4.
[7] S. R. Cloude, "The dual polarization entropy/alpha decomposition: A palsar case study," *Sci. Appl. SAR Polarimetry Polarimetric Interferometry*, vol. 644, 2007, Art. no. 2.
[8] K. Ji and Y. Wu, "Scattering mechanism extraction by a modified Cloude-Pottier decomposition for dual polarization SAR," *Remote Sens.*, vol. 7, no. 6, pp. 7447–7470, 2015.
[9] J. M. Lopez-Sanchez, S. R. Cloude, and J. D. Ballester-Berman, "Rice phenology monitoring by means of SAR polarimetry at X-band," *IEEE Trans. Geosci. Remote Sens.*, vol. 50, no. 7, pp. 2695–2709, Jul. 2012.
[10] D. Mandal et al., "Dual polarimetric radar vegetation index for crop growth monitoring using sentinel-1 SAR data," *Remote Sens. Environ.*, vol. 247, 2020, Art. no. 111954.
[11] S. R. Cloude and E. Pottier, "A review of target decomposition theorems in radar polarimetry," *IEEE Trans. Geosci. Remote Sens.*, vol. 34, no. 2, pp. 498–518, Mar. 1996.
[12] S. R. Cloude and E. Pottier, "An entropy based classification scheme for land applications of polarimetric SAR," *IEEE Trans. Geosci. Remote Sens.*, vol. 35, no. 1, pp. 68–78, Jan. 1997.
[13] S.-E. Park and W. M. Moon, "Unsupervised classification of scattering mechanisms in polarimetric SAR data using fuzzy logic in entropy and alpha plane," *IEEE Trans. Geosci. Remote Sens.*, vol. 45, no. 8, pp. 2652–2664, Aug. 2007.
[14] K. Voormansik, T. Jagdhuber, K. Zalite, M. Noorma, and I. Hajnsek, "Observations of cutting practices in agricultural grasslands using polarimetric SAR," *IEEE J. Sel. Topics Appl. Earth Observ. Remote Sens.*, vol. 9, no. 4, pp. 1382–1396, Apr. 2016.
[15] S.-E. Park and S.-G. Lee, "On the use of single-, dual-, and quad-polarimetric SAR observation for landslide detection," *ISPRS Int. J. Geo-Inf.*, vol. 8, no. 9, 2019, Art. no. 384.
[16] S.-E. Park, Y. Yamaguchi, and D.-j. Kim, "Polarimetric SAR remote sensing of the 2011 Tohoku earthquake using alos/palsar," *Remote Sens. Environ.*, vol. 132, pp. 212–220, 2013.
[17] F. Zhao and J. J. Mallorqui, "Coherency matrix decomposition-based polarimetric persistent scatterer interferometry," *IEEE Trans. Geosci. Remote Sens.*, vol. 57, no. 10, pp. 7819–7831, Oct. 2019.
[18] T. Weiß, T. Ramsauer, T. Jagdhuber, A. Löw, and P. Marzahn, "Sentinel-1 backscatter analysis and radiative transfer modeling of dense winter wheat time series," *Remote Sens.*, vol. 13, no. 12, 2021, Art. no. 2320.
[19] X. Zhou, Z. Zhang, Q. Shen, Q. Chen, and X. Liu, "Identifying soil freeze/thaw states using scattering and coherence time series of high-resolution c-band synthetic aperture radar in the Qinghai-Tibet plateau," *IEEE J. Sel. Topics Appl. Earth Observ. Remote Sens.*, vol. 15, pp. 519–532, 2022.
[20] D. Velotto, C. Bentes, B. Tings, and S. Lehner, "First comparison of Sentinel-1 and terraSAR-X data in the framework of maritime targets detection: South Italy case," *IEEE J. Ocean. Eng.*, vol. 41, no. 4, pp. 993–1006, Oct. 2016.
[21] J. Guo, P.-L. Wei, J. Liu, B. Jin, B.-F. Su, and Z.-S. Zhou, "Crop classification based on differential characteristics of H/alpha scattering parameters for multitemporal quad-and dual-polarization SAR images," *IEEE Trans. Geosci. Remote Sens.*, vol. 56, no. 10, pp. 6111–6123, Oct. 2018.
[22] K. Harfenmeister, S. Itzerott, C. Weltzien, and D. Spengler, "Agricultural monitoring using polarimetric decomposition parameters of sentinel-1 data," *Remote Sens.*, vol. 13, no. 4, 2021, Art. no. 575.
[23] S. Plank, M. Jüssi, S. Martinis, and A. Twele, "Combining polarimetric sentinel-1 and Alos-2/Palsar-2 imagery for mapping of flooded vegetation," in *Proc. IEEE Int. Geosci. Remote Sens. Symp.*, 2017, pp. 5705–5708.
[24] S. De Petris, F. Sarvia, M. Gullino, E. Tarantino, and E. Borgogno-Mondino, "Sentinel-1 polarimetry to map apple orchard damage after a storm," *Remote Sens.*, vol. 13, no. 5, 2021, Art. no. 1030.
[25] Y. N. Lin, Y.-C. Chen, Y.-T. Kuo, and W.-A. Chao, "Performance study of landslide detection using multi-temporal SAR images," *Remote Sens.*, vol. 14, no. 10, 2022, Art. no. 2444.
[26] H. Zhang et al., "Potential of combining optical and dual polarimetric SAR data for improving mangrove species discrimination using rotation forest," *Remote Sens.*, vol. 10, no. 3, 2018, Art. no. 467.
[27] R. Shamshiri, H. Nahavandchi, and M. Motagh, "Persistent scatterer analysis using dual-polarization Sentinel-1 data: Contribution from VH channel," *IEEE J. Sel. Topics Appl. Earth Observ. Remote Sens.*, vol. 11, no. 9, pp. 3105–3112, Sep. 2018.
[28] Wikipedia, 2022 Luding earthquake, 2022. [Online]. Available: https://en.wikipedia.org/wiki/2022_Luding_earthquake
[29] A. Aubry, V. Carotenuto, A. De Maio, and L. Pallotta, "Assessing reciprocity in polarimetric SAR data," *IEEE Geosci. Remote Sens. Lett.*, vol. 17, no. 1, pp. 87–91, Jan. 2020.

[30] Y. Yamaguchi, *Polarimetric SAR Imaging: Theory and Applications*. Boca Raton, FL, USA: CRC Press, 2020.

[31] ESA, Polsarpro (the polarimetric SAR data processing and educational tool), 2019. [Online]. Available: https://earth.esa.int/web/polsarpro/

[32] W. L. Cameron and L. K. Leung, "Feature motivated polarization scattering matrix decomposition," in *Proc. IEEE Int. Conf. Radar*, 1990, pp. 549–557.

[33] R. A. Horn and C. R. Johnson, *Matrix Analysis*. Cambridge, U.K.: Cambridge Univ. Press, 2012.

[34] R. Sabry and P. W. Vachon, "A unified framework for general compact and quad polarimetric SAR data and imagery analysis," *IEEE Trans. Geosci. Remote Sens.*, vol. 52, no. 1, pp. 582–602, Jan. 2014.

[35] W. Hou, F. Zhao, X. Liu, H. Zhang, and R. Wang, "A unified framework for comparing the classification performance between quad-, compact-, and dual-polarimetric SARs," *IEEE Trans. Geosci. Remote Sens.*, vol. 60, 2022, Art. no. 5204814.

[36] L. Liang, Y. Zhang, and D. Li, "Fast Huynen–Euler decomposition and its application in disaster monitoring," *IEEE J. Sel. Topics Appl. Earth Observ. Remote Sens.*, vol. 14, pp. 4231–4243, 2021.

[37] J.-S. Lee and T. L. Ainsworth, "The effect of orientation angle compensation on coherency matrix and polarimetric target decompositions," *IEEE Trans. Geosci. Remote Sens.*, vol. 49, no. 1, pp. 53–64, Jan. 2011.

[38] L. Liang, Y. Zhang, and D. Li, "A novel method for polarization orientation angle estimation over steep terrain and comparison of deorientation algorithms," *IEEE Trans. Geosci. Remote Sens.*, vol. 59, no. 6, pp. 4790–4801, Jun. 2021.

[39] A. C. Cameron and F. A. Windmeijer, "An r-squared measure of goodness of fit for some common nonlinear regression models," *J. Econometrics*, vol. 77, no. 2, pp. 329–342, 1997.

[40] X. Liu et al., "PolSF: PolSAR image dataset on San Francisco," in *Proc. Int. Conf. Intell. Sci.*, 2022, pp. 214–219.

[41] T. Caliński and J. Harabasz, "A dendrite method for cluster analysis," *Commun. Statist.-Theory Methods*, vol. 3, no. 1, pp. 1–27, 1974.

[42] D. Arthur et al., "K-means : The advantages of careful seeding," *Soda*, vol. 7, 2007, pp. 1027–1035.

[43] J. R. Huynen, "Phenomenological theory of radar targets," Ph.D. dissertation, *Dept. Elect. Eng., Math. Comput. Sci., Tech. Univ. Delft*, Delft, The Netherlands, 1970.

[44] D. Li and Y. Zhang, "Unified Huynen phenomenological decomposition of radar targets and its classification applications," *IEEE Trans. Geosci. Remote Sens.*, vol. 54, no. 2, pp. 723–743, Feb. 2016.

[45] Q. Chen, G. Kuang, J. Li, L. Sui, and D. Li, "Unsupervised land cover/land use classification using polsar imagery based on scattering similarity," *IEEE Trans. Geosci. Remote Sens.*, vol. 51, no. 3, pp. 1817–1825, Mar. 2013.

[46] Z. Zhang, H. Wang, F. Xu, and Y.-Q. Jin, "Complex-valued convolutional neural network and its application in polarimetric SAR image classification," *IEEE Trans. Geosci. Remote Sens.*, vol. 55, no. 12, pp. 7177–7188, Dec. 2017.

[47] Y. An et al., "Preliminary report of the september 5, 2022ms 6.8 Luding earthquake, Sichuan, China," *Earthq. Res. Adv.*, vol. 3, no. 1, 2023, Art. no. 100184.

[48] Y. Huang et al., "An open-accessed inventory of landslides triggered by the ms 6.8 Luding earthquake, China on Sep. 5, 2022," *Earthq. Res. Adv.*, vol. 3, no. 1, 2023, Art. no. 100181.

[49] J. Zhang et al., "Distribution patterns of landslides triggered by the 2022ms 6.8 Luding earthquake, Sichuan, China," *J. Mountain Sci.*, vol. 20, no. 3, pp. 607–623, 2023.

[50] L. Bruzzone and D. F. Prieto, "Automatic analysis of the difference image for unsupervised change detection," *IEEE Trans. Geosci. Remote Sens.*, vol. 38, no. 3, pp. 1171–1182, May 2000.

[51] Xinhuanet, "Luding earthquake: Rescue on the Dadu river," 2022. [Online]. Available: http://www.news.cn/2022-09/09/c_1128991509.htm

[52] ESA, "Absolute radiometric and polarimetric calibration of ALOS PALSAR products generated with Aden," 2009. [Online]. Available: https://earth.esa.int/eogateway/documents/20142/37627/ALOS-PALSAR-calibration-products-ADEN.pdf

[53] Y. Tang et al., "An object fine-grained change detection method based on frequency decoupling interaction for high-resolution remote sensing images," *IEEE Trans. Geosci. Remote Sens.*, vol. 62, 2023, Art. no. 5600213.

[54] C. Zhao et al., "Hyperspectral image classification with multi-attention transformer and adaptive superpixel segmentation-based active learning," *IEEE Trans. Image Process.*, vol. 32, pp. 3606–3621, 2023.

[55] C. Zhao, W. Zhu, and S. Feng, "Superpixel guided deformable convolution network for hyperspectral image classification," *IEEE Trans. Image Process.*, vol. 31, pp. 3838–3851, 2022.

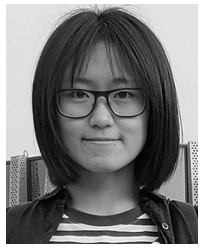

Liting Liang (Member, IEEE) received the B.S. degree in electronic information engineering from the Harbin Engineering University, Harbin, China, in 2016 and the Ph.D. degree in electromagnetic field and microwave technology from the University of Chinese Academy of Sciences, Beijing, China, in 2021.

She is currently a Postdoctoral Researcher with the CAS Key Laboratory of Microwave Remote Sensing, National Space Science Center, Chinese Academy of Sciences, Beijing, China. Her research interests include synthetic aperture radar (SAR) polarimetry, polarimetric scattering modeling and decomposition, and applications of polarimetric radar remote sensing.

Dr. Liang was the recipient of the President Award (excellent prize) of the Chinese Academy of Sciences in 2021.

Yunhua Zhang (Member, IEEE) received the B.S. degree from Xidian University, Xi'an, China, in 1989 and the M.S. and Ph.D. degrees from Zhejiang University, Hangzhou, China, in 1993 and 1995, respectively, all in electrical engineering.

He is currently a Professor with the National Space Science Center, Chinese Academy of Sciences, Beijing, China, and the Director of the CAS Key Laboratory of Microwave Remote Sensing. He is also a Professor with the School of Electronic, Electrical and Communication Engineering, University of Chinese Academy of Sciences, Beijing, where he lectured modern radar theory and technology to the postgraduate students. He is the Chief Designer for the Chinese Tiangong-2 Interferometric Imaging Altimeter, which is the first spaceborne wide-swath radar altimeter launched in September 15, 2016. His research interests include the system design and signal processing of microwave sensors (high-resolution radar, interferometric radar, radar altimeter, and noise radar), polarimetric radar target decomposition, application of compressive sensing in radar, and antennas and computational electromagnetics.

Dong Li (Member, IEEE) received the B.S. degree in electronic engineering from Xidian University, Xi'an, China, in 2008 and the Ph.D. degree in electrical engineering from the University of Chinese Academy of Sciences, Beijing, China, in 2013.

He is currently an Associate Professor with the CAS Key Laboratory of Microwave Remote Sensing, National Space Science Center, Chinese Academy of Sciences, Beijing. His research interests include synthetic aperture radar (SAR) polarimetry, polarimetric target decomposition, polarimetric scattering modeling, SAR image registration, and computer SAR vision.

Dr. Li was elected as a Member of the Youth Innovation Promotion Association, Chinese Academy of Sciences in 2014. He received the President Scholarship for Outstanding Students of Chinese Academy of Sciences in 2013 for his Ph.D. dissertation on the stereo processing and polarimetric analysis of SAR images.

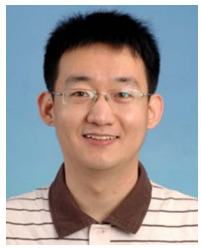

Xiao Dong (Member, IEEE) received the B.S. degree from Xidian University, Xi'an, China, in 2009, and the Ph.D. degree from the University of Chinese Academy of Sciences, Beijing, China, in 2015, respectively, all in electrical engineering.

He is currently an Associate Professor with National Space Science Center, Chinese Academy of Sciences, Beijing, China. His research interests include signal processing and radar imaging.